Fall 12-19-2020

Modeling Fluid Phenomena in the Context of the Constrained Vapor Bubble System

James Barrett
jabarrett@smu.edu

MODELING FLUID PHENOMENA IN THE CONTEXT OF THE CONSTRAINED VAPOR BUBBLE SYSTEM

Approved by:

Dr. Vladimir Ajaev,
Professor of Mathematics

Dr. Sheng Xu,
Associate Professor of Mathematics

Dr. Daniel Reynolds,
Professor of Mathematics

Dr. David Willis,
Associate Professor of Mechanical Engineering

MODELING FLUID PHENOMENA IN THE CONTEXT OF THE CONSTRAINED VAPOR BUBBLE SYSTEM

A Dissertation Presented to the Graduate Faculty of the

Dedman College: School of Humanities and Sciences

Southern Methodist University

in

Partial Fulfillment of the Requirements

for the degree of

Doctor of Philosophy

with a

Major in Computational and Applied Mathematics

by

James A. Barrett

B.S., Brigham Young University-Idaho
M.S., Southern Methodist University

December 19, 2020

ACKNOWLEDGMENTS

Primarily, I would like to thank my thesis adviser, Dr. Ajaev, for his continued support and mentorship. He provided insight, opportunity and encouragement all along the way. Completing my work here wouldn't have been possible without his advice and help.

I would also like to thank the Department of Mathematics of Southern Methodist University and my excellent professors who took great care to support me despite taking a leave of absence to be with family during a crisis, and for welcoming me back to finish what I started. Dr. Reynolds for instilling in me a keen interest of numerical methods and to not be satisfied with working code but to enjoy the push for faster more accurate code. Dr. Norris who took time to look in on me and my group of first year students staying late working on homework to encourage and help. Dr. Aceves for his departmental leadership and warm welcome to the math office. Our math department secretary Liz Berry for always having an answer and the occasional free food to shorten a long day.

Funding from the National National Aeronautics and Space Administration also made this research possible, so that I could focus on the needed research to complete this work.

Lastly, My wife Tasheena who tirelessly handled everything at home with our four energetic children. While I tried desperately to find a quite place to work from home during the Covid-19 pandemic. I couldn't have done it without you.

Barrett , James A.

B.S., Brigham Young University-Idaho
M.S., Southern Methodist University

Modeling Fluid Phenomena in the Context of the
Constrained Vapor Bubble System

Advisor: Professor Vladimir Ajaev
Doctor of Philosophy degree conferred December 19, 2020
Dissertation completed December 19, 2020

This thesis focuses on the fluid phenomena observed within what is known as the constrained vapor bubble system. The constrained vapor bubble system is a closed system consisting of a quartz cuvette partially filled with liquid and used as a coolant device. Heat is applied to the heater end which causes the liquid to evaporate and condense on the cooled end of the cuvette. Liquid travels back to the heated end via capillary flow in the corners. A pure vapor bubble is formed in the center of the cuvette giving rise to the name of the experiment. The constrained vapor bubble system is important due to its potential use for cooling devices in microgravity since it does not require a metal wick or gravity used by most micro heat pipes. Experiments done onboard the International Space Station showed fluid phenomena inconsistent with mathematical models and experiments performed in earth's environment. Most notably a flooded heater end and droplets forming on the four walls of the cuvette. 1-dimensional and 2-dimensional heat transfer models are presented.

Novel mathematical models of heat transfer and fluid flow in the constrained vapor bubble system are developed in the thesis. Fitting the experimental data from [11] to the 1D heat transfer model in the region near the hot end leads to an estimate of the internal heat transfer coefficient of 400 W/(m^2 K) there. However, the heat transfer coefficient is found to increase in the condensation zone near the middle of the cuvette, an observation explained by increased liquid-vapor interface area. Finally, near the cold end the heat transfer is

dominated by axial conduction in the liquid phase that fills most of the cross-section and the heat transfer coefficient drops to zero. In the 2D cross-sectional model for temperature the evaporative flux is calculated by taking into account heat transfer in the liquid phase in the corners of the cuvette and introducing a localized cooling parameter into the boundary conditions at the cuvette walls. Heat flux at the liquid-vapor interface is determined and used to estimate the evaporative loss and thus the axial velocity of the flow, with typical average axial flow velocity found to be of the order of 1 mm/s. An analytical estimate of flow velocity is obtained and is shown to be consistent with the numerical results. Effects of 3D heat conduction in the cuvette and the Marangoni stresses are also studied. Further investigation is needed to fully understand the mechanisms of the flow slow-down in the evaporation region.

A mathematical model is developed of an evaporating droplet observed in the constrained vapor bubble experimental set-up. The motion of receding contact line is described using two-component disjoining pressure coupled with the effects of phase change and capillarity. The results include dynamics of interface shapes during droplet evaporation, including the radius of curvature at the top of the droplet expressed in dimensional form. The evaporative flux is found to increase toward the contact line, but not as sharply as in the case of evaporating meniscus due to the addition of localized cooling of the substrate. Detailed studies of the the effect of evaporative cooling parameter K_s on the solutions are conducted. Increase in K_s leads to lower local heat flux near the contact line and thus slower evaporation. Radius of curvature at the top of the droplet is found to decrease in a linear fashion with the slope consistent with experimentally measured values. A second term in the disjoining pressure gives excellent control over contact angle for matching with experiments or observing different regimes.

TABLE OF CONTENTS

LIST OF FIGURES

LIST OF TABLES

To my family Tasheena, Owen, Joey, Thea and Kincaid. Also my parents Kevin and Jenny, who knew I'd go far even when I couldn't see it.

Chapter 1

INTRODUCTION: THE CONSTRAINED VAPOR BUBBLE SYSTEM

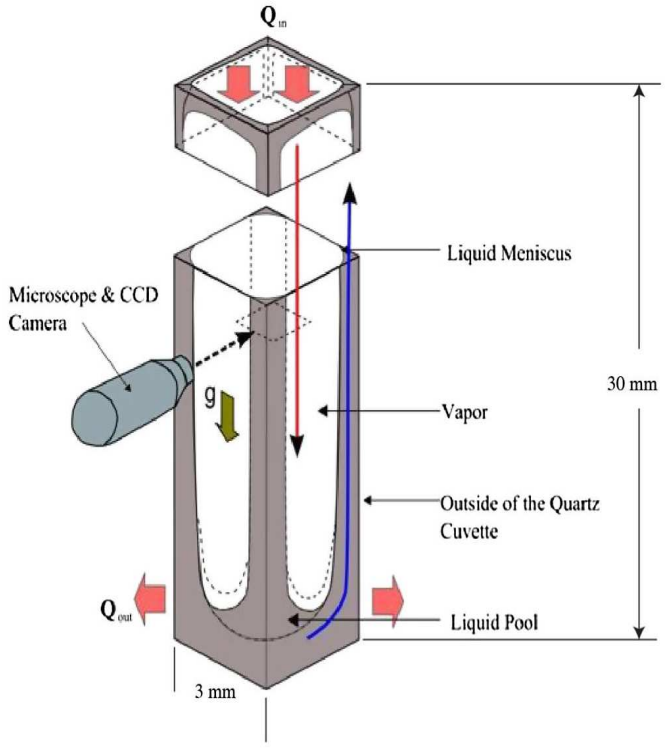

Figure 1.1: Diagram of the Constrained Vapor Bubble system.

The focus of this thesis is centered on modeling of the heat transfer of the constrained vapor bubble (CVB) system designed by the group of J. Plawsky [11] and the fluid phenomena observed within the system pictured in Figure 1.1. It is important to have a clear understanding of the system and the previous work that this thesis will build on. In the CVB system, liquid-vapor mixture inside an elongated cuvette of rectangular cross-section is subject to axial temperature gradients resulting in phase change and complex flow patterns.

Mathematical models of the CVB often rely on wedge flow models developed for micro heat pipes. Introduced by Cotter [13], these devices are notable for their applications for

cooling and have generated interest for their efficiency at transferring large amounts of heat and most notably use in microgravity applications. Micro heat pipes rely on circulation of fluid from cold regions to heated regions via capillary forces negating the need for external forces such as pumps to transport heat into the region where evaporation takes place. In most micro heat pipes a metal component, called a wick, helps in facilitating the capillary flow. These metal wicks designed with specific structure in mind strengthen the effect of capillary flow. The CVB however, does not rely on a wick, allowing it to be lighter and more versatile for use in microgravity applications. Fluid transport in wickless heat pipes often occurs in V-shaped wedges and the majority of modeling is focused on the fluid flow and heat transfer in these wedges.

1.1. Background on modeling for the CVB

The early wedge flow models began with Babin et al. [7] who focused on the relationship between the mean curvature of the liquid-vapor interface and the hydraulic radius of the flow channel. In micro heat pipes, the hydraulic radius of the flow channel divided by the capillary radius is less than or equal to 1, and capillary forces are assumed to be the driving force of fluid flow. Babin et al. [7] determined many working parameters of micro heat pipes including steady state performance limitations on the fluid to vapor ratio, shape of the structure, operating temperature, evaporative flux, and the effects of gravity. Building on these results, Wu and Peterson [46] investigated further important parameters in the efficiency of micro heat pipes, most notably, the influence of wetting angle on the heat pipes' ability to transfer heat. They compared their model to previous experimental results and looked at the difference in heat transfer for the wetting angles of 0 and 45 degrees. Qualitatively different axial pressure profiles were predicted by the model for the different wetting angles. Xu and Carey [47] made the important distinction of evaporation occurring mainly at the apparent contact line, which is consistent with other literature on evaporating menisci. This study uses a two part solution focusing on disjoining pressure as the driving force near the contact line and capillary forces dominating the interface shapes in the meniscus region.

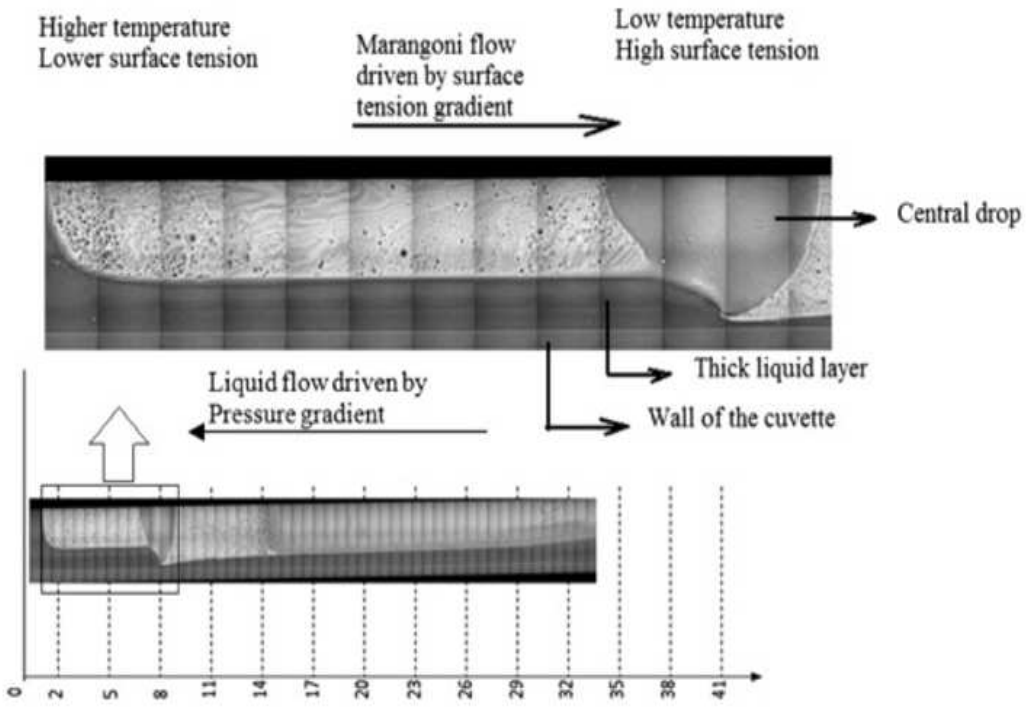

Figure 1.2: Photograph of the heated end of the CVB depicting the role of Marangoni flow[24].

The work of Swanson and Peterson [45] followed with a model including the effects of both disjoining pressure and Marangoni stresses. Marangoni flow occurs in the presence of surface tension gradients as liquid flows from areas of low surface tension to high surface tension as illustrated in the work from Kundan et al. [24] in Figure 1.2. Surface tension gradients occur due to the changes in temperature along the menisci with lower surface tension at higher temperatures and higher surface tension at lower temperatures. This change in surface tension creates a flow from the heated end to the cooled end acting in contrast to the capillary driven flow, and is believed to be an important contribution to the flow in the corners. Their model focused on a triangular shaped design with three wedges, rather than the current 4 wedge square design that is currently used, and accounted for the presence of a non-evaporating adsorbed film that occurs between corner menisci and at the heated end of the micro heat pipe under dry out conditions.

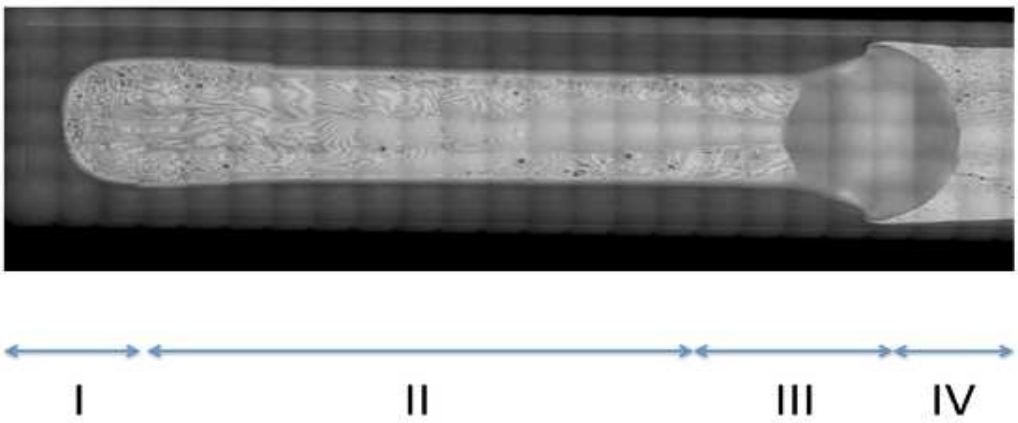

Figure 1.3: Complex liquid-vapor interface shape seen in the CVB, separated into sections for heat transfer and fluid flow modeling[25].

More recent works([48, 30, 42]) emphasized the importance of Marangoni flow illustrating that Marangoni forces could drive liquid away from the heater end in conflict with capillary forces leading to a dryout condition. For example, Savino and Paterna [42], through an analytical-numerical study showed that the choice of fluid was instrumental in the efficiency of the wedge flow to transfer heat. They found that using some binary mixtures is preferable to water. While Yang and Homsy [48] presented a comprehensive model of a steady state configuration for wedge flow in a corner under both Marangoni and capillary flow. Their main result was in relation to the size of the wedge angle and its effect on dryout. They found that dryout was typically more easily obtained for larger wedge angles. Lastly, Markos et al. [30] determined the optimal wedge angle for the capillary flow into the evaporator region of the heat pipe and showed the potential for Marangoni stresses to interact with capillary forces and move the dry-out location away from the heated end.

The experiments conducted in microgravity aboard the International Space Station reported by Chatterjee et al. [11] and Kundan et al. [25] presented a complex picture of fluid flow and heat transfer in the CVB. Figure 1.3 shows the interface shape in the heated end of the cuvette from this experimental study split into four sections to simplify the analysis. Each square in the image measures 0.5mm as illustrated in Figure 1.4[10]. This measurement is used to determine the lengths of the sections for later analysis. Section I shows

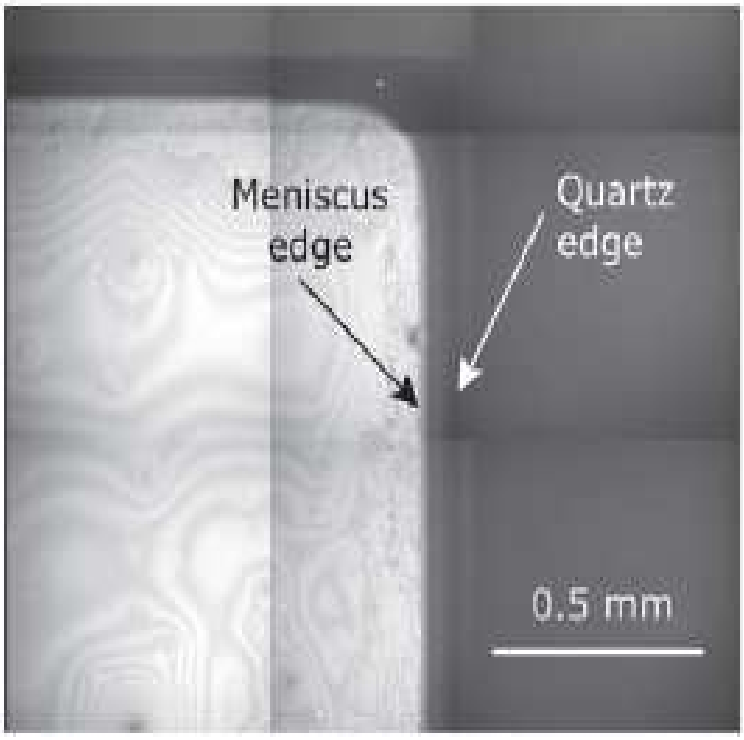

Figure 1.4: Close up photograph of the corner of the CVB to help in visualizing measurements from Figure 1.3.

the flooded region where, despite the elevated temperature, the liquid remained trapped in the heated end unable to reach evaporation levels high enough to result in a flow to the colder regions as previous models and experiments in Earth's environment expected [10]. In section II there is very little change to the cross-sectional interface shape for a significant portion of the heat pipe. Section III shows what is referred to in the literature as the center drop (or possibly four drops, one on each wall of the cuvette) with a significant pinching of the corner wedge flow where it interacts with the droplet. The mechanism of formation of the center drops is not fully understood. One explanation given by Kundan et al. [24] is that the competition between opposing capillary flow toward the heated end and Marangoni flow toward the cold region causes the liquid to spill out of the wedge forming these center drops. The final section, section IV, illustrates the capillary driven flow predicted by the aforementioned models of micro heat pipes. The majority of the models in this thesis will focus on the dynamics seen in section II which correlates e.g. to the 6 mm section of the

40 mm heat pipe from 3 mm to 9 mm. Because of the complexity of the flooded region occurring in sections I-III of the cuvette, as well as lack of direct experimental investigations of the flow patterns, relatively little is known about the actual flow in this region.

1.2. Background on droplet evaporation

The complex nature of the physical phenomena observed in the constrained vapor bubble set-up leads to simplifying the system by focusing on individual aspects of the fluid dynamics. The heat transfer models, for example, will emphasize heat transfer occurring and fluid flow in section 2 illustrated in Figure 1.3. Droplets observed on the cuvette quartz walls between the liquid wedge flows near the heated end of the cuvette [19, 11] will be the focus of the latter portion of this thesis.

The study of droplets and droplet evaporation have been a focus of study under the umbrella of lubrication theory pioneered by Reynolds in 1886 [40]. Lubrication theory has been essential to our modern understanding of moving liquid vapor interfaces. At its core Lubrication theory simplifies the Navier-Stokes equations to a more manageable system of differential equations by taking advantage of length scale differences. Lubrication theory is applicable in any situation where one length scale is much smaller than another. For example with the air flow over an air hockey table the vertical length scale of the air is much smaller than the horizontal. The approach taken in Chapter 4 will illustrate the use of lubrication theory to model the moving interface of an evaporating droplet observed in the CVB.

Since the introduction of lubrication theory, researchers have used it in a number of fields, from geophysics with Huppert's work [21] in gravity flows and Ancey's work in geophysical flows [5] to nanotechnology investigated by Eijkel and Van Den Berg [18]. Lubrication theory is now being used in applications for heat transfer for space application via the CVB. For droplet evaporation we build off of the work using these lubrication type models with an emphasis on the physics occurring in the droplet. Burelbach et al. [9] introduced the idea of focusing on the effects in the fluid rather than the vapor noting that the effects seen in the vapor could be neglected and that the nonequilibrium effects at the free surface of the

droplet are the rate-limiting evaporative process.

Several studies followed this approach such as Davis and Anderson [6] who introduced a 2D model focused on the effects of evaporation and contact line dynamics. They also proposed different capillary regimes, where large capillary numbers resulted in tall skinny droplets resisting evaporation and small capillary numbers resulting in thin quickly evaporating droplets. The thicker the droplet they found shortened evaporation time.

Ajaev [1] followed by introducing use of an adsorbed film to handle the contact line singularity. His study also moved outside the steady-state configuration allowing for motion of the contact line. Through the use of the moving contact line Ajaev was able to introduce results leading to the conclusion that evaporation and spreading tend to compete. In other words, evaporation tends to prevent spreading. Finally, he introduces an axisymetric lubrication type model for evaporation which is a large focus of Chapter 4.

Sodtke et al. [44] followed up on the previous two studies by introducing a second term to disjoining pressure to account for electrostatic effects similar to that done in Chapters 4 and 5. This study was unique in that it was created as a collaboration between experimentalists and mathematicians, which allowed for direct comparison of the mathematical modeling with experimental observation. An important finding that resulted in future changes to the model was in the discovery of a sharp decline in temperature at the contact line suggesting the need for localized cooling of the substrate. This localized cooling is introduced in Chapter 2 and used in the model introduced in Chapter 4 as well.

Near the contact line of evaporating droplets where film thickness is smallest the interaction with the substrate becomes more important. The approach used in this thesis is through disjoining pressure which describes the interaction between molecules in the fluid and the substrate and was introduced by Derjaguin et al. [17]. It is typically described in mathematical models by the London van-der Waals dispersion forces which are larger when the separation between atoms is large, and considerably weaker when the distance from the substrate to the liquid vapor interface is greater. Potash and Wayner [39] used the Hamaker constant over the thickeness of the thin film to model these forces. However, this definition

of the disjoining pressure becomes problematic when the film thickness approaches zero resulting in abnormally large values of the disjoining pressure. One approach, taken by Yi and Wong [49] for example, initiates a slope-dependent disjoining pressure to alleviate this singularity near the contact line. This approach is especially valuable in equilibrium conditions with nonvolatile droplets. The approach taken in this thesis to avoid the singularity due to small film thickness near the contact line is to include a precursor or adsorbed film as done by Ajaev [1].

Chapter 2

HEAT TRANSFER MODELING

2.1. 1D approach for axial heat conduction and losses

Let us now discuss the outline of the modeling approaches developed in the present chapter and how they address the existing gaps in the literature. We first focus on heat transfer in the cuvette. Though Kundan et al. [25] and Chatterjee et al. [11] developed an accurate model of heat transfer in the walls of the cuvette, key limitations of their work include the assumptions of a constant heat transfer coefficient along the entire cuvette and accounting for temperature variation only in the axial direction of the cuvette so that the model is essentially one-dimensional.

We overcome both of these limitations, first by incorporating axial variations of the heat transfer coefficient into the 1D framework and then developing numerical heat transfer models which account for the full three-dimensional geometry of the cuvette. The nature of the fluid flow in CVB has been addressed only qualitatively in the previous studies [11, 25]. We use the detailed information about heat transfer to estimate evaporative mass loss at the interface and thus infer meaningful results about the fluid flow, most notably the changes in axial velocity of flow along the cuvette. The significance of Marangoni stresses is also discussed.

Our first objective is to understand heat transfer at the walls of the cuvette. We start by modifying the model for dimensional temperature T^* used by Chatterjee et al. [11], usually written in the form

$$k_q A_q \frac{d^2 T^*}{dz^2} = k_a p_o \frac{T^* - T_\infty}{D} + \sigma_B \epsilon p_o (T^{*4} - T_\infty^4) + h_i p_i (T^* - T_s^*). \tag{2.1}$$

Table 2.1: Parameter values for CVB

Cross sectional area of the cuvette	$A_q = 21.25$ mm^2
Inner cross-section perimeter	$p_i = 12$ mm
Outer cross-section perimeter	$p_o = 22$ mm
Thermal conductivity of quartz	$k_q = 1.46$ W m^{-1}K^{-1}
Thermal conductivity of air	$k_a = 0.026$ W m^{-1}K^{-1}
Outside wall temperature	$T_\infty = 293.15$ K
Distance to outside wall	$D = 63.5$ mm
Stefan-Boltzmann constant	$\sigma_B = 5.67 \times 10^{-8}$ W m^{-2}K^{-4}
Emissivity of quartz	$\epsilon = 0.93$
Gas constant per unit mass	$\bar{R} = 115.2$ J kg^{-1}K^{-1}

The model is formed from the standard 1D steady state heat equation with three additional terms: two accounting for the heat loss at the outside wall of the cuvette through conduction into air and the other for radiation heat loss, and the third for internal heat flux. Here k_q and k_a are the thermal conductivities of the quartz cuvette and air respectively while h_i is the internal heat transfer coefficient. A_q is the cross sectional area of the cuvette with dimensions 5.5 x 5.5 mm on the outside and 3 x 3 mm on the inside. T_∞ is the temperature at the outside wall containing the CVB experimental set up, and T_s^* is the saturation temperature of the liquid. The parameter D is the distance from the quartz cuvette to the outside wall which we have set to 63.5 mm to match with the experimental setup. The coefficients on the radiation term are σ_B, ϵ, p_o, and p_i which are the Stefan-Boltzmann constant, emissivity of quartz, and the outer and inner wetting perimeters respectively. All of these are known quantities with the exception of the internal heat transfer coefficient h_i. Relevant values for the parameters which are either independent from or weakly dependent on temperature are recorded in Table 2.1.

The model based on equation (2.1) allowed Chatterjee et al. [11] and Kundan et al. [25] to obtain useful estimates of the average heat transfer coefficient by minimizing the error between the data obtained from equation (2.1) and the experimental data. The temperature profiles based on this model can be used to fit parts of the measured temperature profile but not the entire profile along the full length of the cuvette. We believe the difficulty in matching the temperature profiles has to do with the fact that the internal heat transfer coefficient is not constant along the cuvette. This is supported by optical observations showing significant changes in the cross-sectional shape of the liquid domain and the volume fraction of the liquid between the different locations along the cuvette, as seen in Figure 1.3. Such changes can lead to axial variation of the heat transfer coefficient as shown e.g. in the context of flow boiling in minichannels for different gravity levels by Luciani et al. [28]. They found that lower percentage of vapor bubbles in the observed flow pattern leads to a locally higher heat transfer coefficient.

To account for axial changes in geometric configuration in CVB, we propose to modify the heat transfer model by relaxing the assumption of the internal heat transfer coefficient, h_i, being constant. Furthermore, in contrast to the previous studies, we do not adjust the value of the coefficient in the region near the heater when the power changes. Remarkably, near the hot end all temperature data we investigated fits the numerical profiles from the model for the same value of the heat transfer coefficient, as illustrated by blue lines in the left part of Figure 2.1. We compared the model to the data from the thermocouples at heater powers of 2.0 W, 1.2 W, and 0.8 W. Several physical properties are different for these cases due to changes in the temperature; these are summarized in Table 2. The value h_i in the region studied here is estimated from the data to be near 400 W/(m^2 K). Note that this does not contradict the lower estimates, between 100 and 350 W/(m^2 K) obtained by Kundan et al. [25] since these authors considered effective value for the entire length of the cuvette, thus incorporating the data from the regions where heat transfer coefficient is lower.

The temperature data shows nearly linear decay of temperature near the cold end of the cuvette, as seen in Figure 2.1. If we assume the heat transfer model based on equation (2.1)

to be valid, the data can be still be fit to the prediction of the model, as shown by the blue lines in the right side of Figure 2.1, but the value of the internal heat transfer coefficient ends up being zero. We believe this result is due to the fact that phase change is no longer the dominant mechanism of internal heat loss as the cross-section fills with liquid and most axial heat transfer is by heat conduction or convection through that liquid. This suggestion is also supported by the fact that straight lines have increasing slope magnitude as the heater power is increased. This is what one would expect for a cuvette completely filled with liquid.

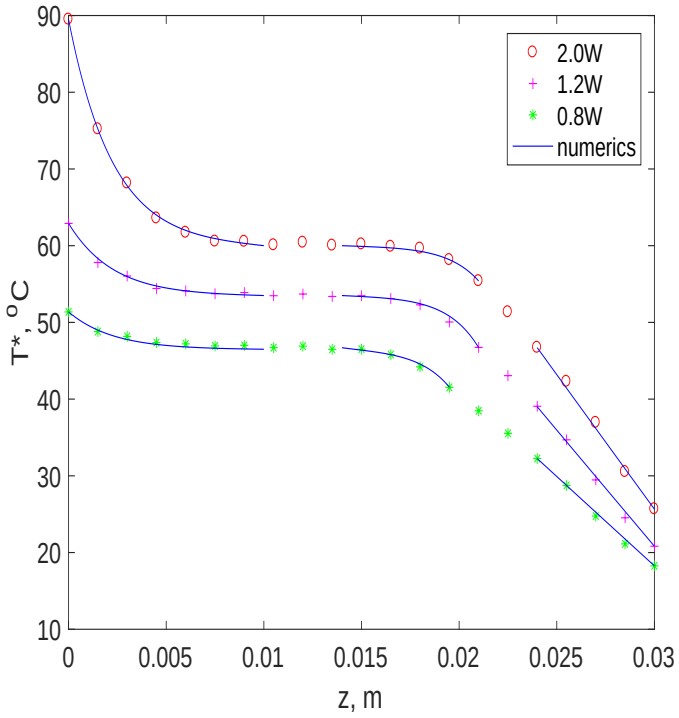

Figure 2.1: Comparison of the 1D heat transfer models predictions and experiments along the length of the 30 mm quartz cuvette.

There is also a transition region from the constant temperature in the middle to the linear regime near the cold end. One might expect the heat transfer coefficient there to be close to the one near the hot end due to similarity of geometric configurations of the cross-sections, as seen in optical observations. However, the curves obtained from our numerical procedure applied in this transition region, shown in Figure 2.1, suggest a value of h_i 2 to 3 times as large as near the heated end. We believe this discrepancy is most likely due to the presence

of thin liquid films on the walls so that condensation can take place there in addition to the corner regions.

To better understand why and how the internal heat transfer coefficient can change along the axial direction without detailed description of the three-dimensional geometry of the problem, let us consider an analogy with a classical configuration in which a film of uniform thickness h is used to cool a region of the hot surface of length L and width w. If the temperature drop ΔT across the film is constant and the non-equilibrium effects on the interface are negligible, the heat flux across the film is given by $\Delta T/h$. This suggests that decreasing film thickness leads to improvement in heat transfer. However, this is a good approximation only for high conductivity substrates, e.g. thick metal plates. Our previous work showed that such an approximation is not likely to be satisfied in the CVB [8]. A more realistic expression would be in the form $\Delta T/(K_s^* + h)$, where the coefficient K_s^* accounts for the effects of heat conduction in the substrate. For these types of models, the key quantity is the area from which evaporation/condensation takes place, and this area increases when there is more liquid in the cross-section. Another interpretation of the same phenomenon could be to say that more coverage of side walls by liquid provides much better heat transfer than dry solid surface in contact with vapor.

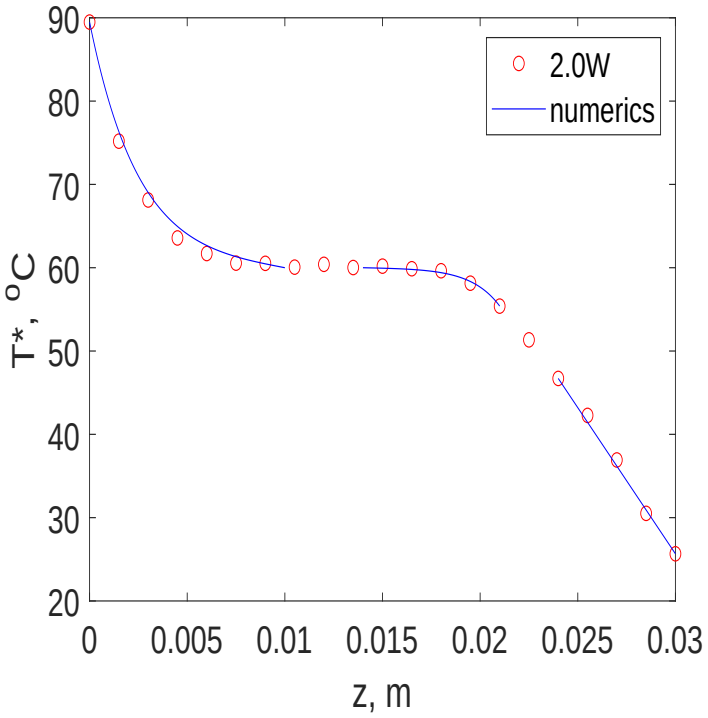

Figure 2.2: Comparison of the 1D heat transfer model to experiment with zero external heat loss at 2.0W heater power.

It is of note that the internal heat transfer component of equation (2.1) is the dominate term and that the matching with experiment is still in good agreement as shown in Figure 2.2. This Figure is obtained by zeroing out the external heat transfer terms by setting the outer wetting perimeter to zero. The biggest deviance from Figure 2.1 is in the 1st region where temperature is highest. This can be explained by the high temperature change to the external environment, where as the rest of the cuvette the internal temperature difference becomes dominate.

Upon further investigation it appears that out of the two external heat transfer terms, namely radiation and conductivity into air, the radiation term seemed to have the larger influence on the heated region as shown in Figure 2.3. The infinity norm error between the full model used to match the experimental data was 0.99. Removing the air conduction heat transfer however, had a minimal change in the heat transfer model as presented in Figure 2.4. The change is imperceptible with an infinity norm error of 0.06. This illustrates the

importance of and thus the focus of this section on the internal heat transfer instead of focusing on the external heat transfer.

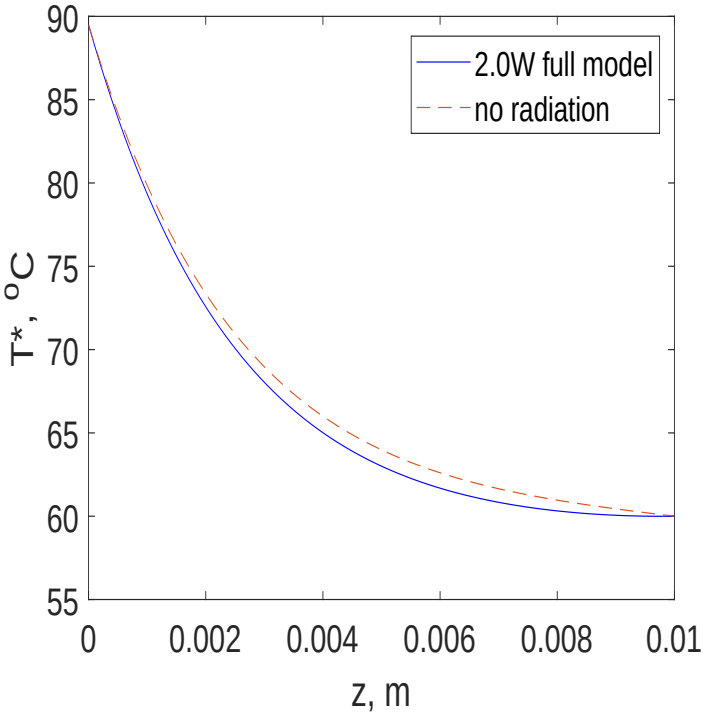

Figure 2.3: Comparison of the full 1D heat transfer model to the model excluding the effects of radiation heat loss.

Table 2.2: Temperature-dependent parameter values for heater powers of 0.8W, 1.2W, and 2.0W

Saturation Temperature	46.5°C	53.5°C	60°C
Thermal conductivity of pentane	$k = 0.104$ W m^{-1}K^{-1}	$k = 0.100$ W m^{-1}K^{-1}	$k = 0.098$ W m^{-1}K^{-1}
Kinetic parameter	$K = 2.38 \times 10^{-5}$	$K = 1.93 \times 10^{-5}$	$K = 1.70 \times 10^{-5}$
Vapor density	$\rho_v = 3.99$ kg m^{-3}	$\rho_v = 5.16$ kg m^{-3}	$\rho_v = 6.19$ kg m^{-3}
Latent heat of vaporization	$\mathcal{L} = 3.47 \times 10^5$ J kg^{-1}	$\mathcal{L} = 3.38 \times 10^5$ J kg^{-1}	$\mathcal{L} = 3.30 \times 10^5$ J kg^{-1}
Viscosity	$\mu = 2.28 \times 10^{-4}$ N s m^{-2}	$\mu = 2.19 \times 10^{-4}$ N s m^{-2}	$\mu = 2.12 \times 10^{-4}$ N s m^{-2}

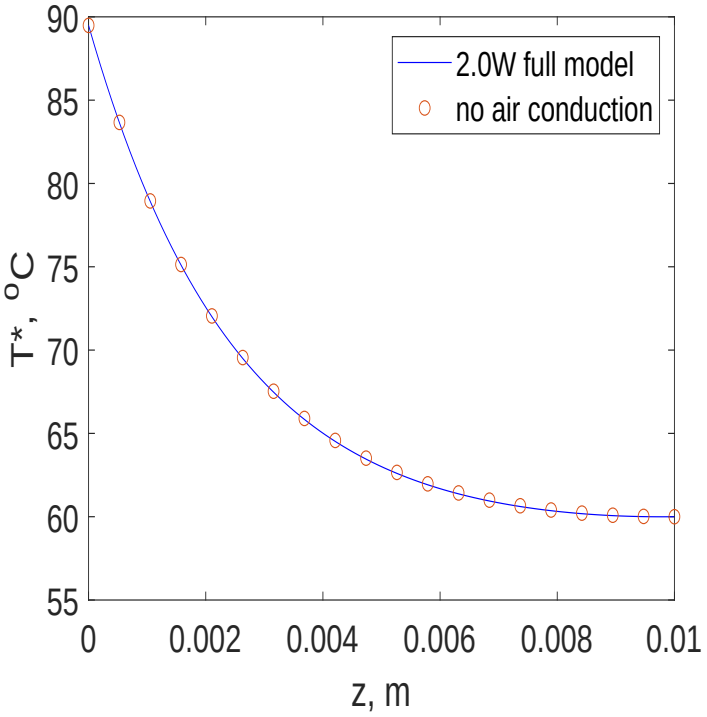

Figure 2.4: Comparison of the full 1D heat transfer model to the model excluding the effects of heat loss due to conduction into air.

2.2. 2D cross-sectional heat transfer

For the purpose of better understanding of how evaporation affects the internal heat transfer coefficient and liquid mass loss, we now consider a 2D cross-section of the corner flow sketched in Figure 2.5. For simplicity we focus on section II, which has the simplest and most approachable geometry. However, since in the steady-state configuration heat and mass transfer in different sections of the cuvette are coupled together, we expect that our

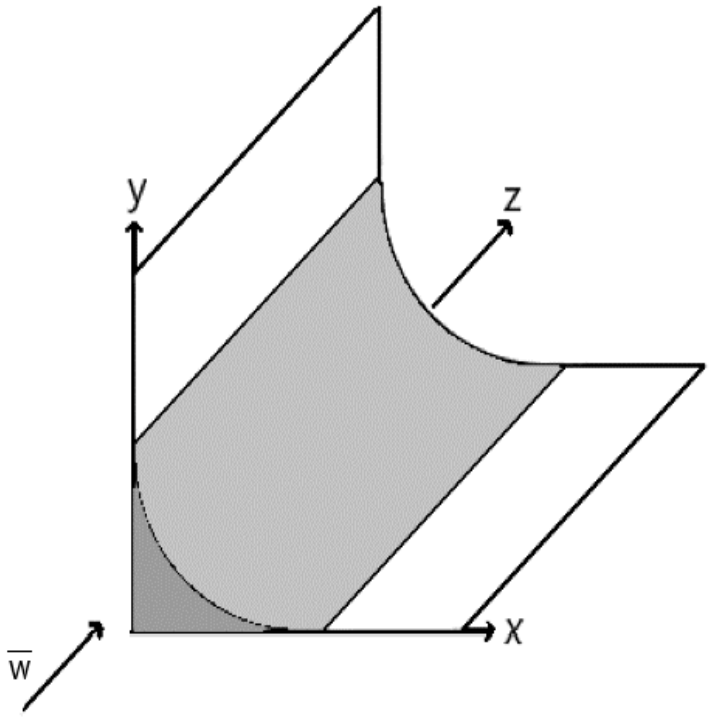

Figure 2.5: Sketch of the corner geometry with the assumption of liquid cross-sectional shape being independent of the axial coordinate z, as relevant for section II in Figure 1.3.

results will provide insights into the global picture of processes taking place in the CVB experiment. We first introduce the nondimensional temperature defined by

$$T = \frac{T^* - T_s^*}{T_s^*}. \tag{2.2}$$

Motivated by optical observations of e.g. section II in Figure 1.3, we assume the liquid-vapor interface to be circular and of the same radius for all cross-sections, as seen in the sketch in Figure 2.5. The contact angle is taken to be zero, motivated by very small measured values of the contact angle for pentane on quartz. We use the following nondimensional 2D Laplace's equation governing the heat transfer in the liquid,

$$\frac{\partial^2 T}{\partial x^2} + \frac{\partial^2 T}{\partial y^2} = 0. \tag{2.3}$$

This approximation is based on the assumption that the axial length scale of temperature variation is much larger than the cross-sectional dimensions. We define the Peclet number as

$$Pe = \frac{UL}{\kappa} \tag{2.4}$$

where U is the characteristic velocity of the fluid, L is the characteristic length scale of the temperature gradient, and $\kappa = k/\rho C$ is the thermal diffusivity. Where k is the thermal conductivity of pentane as previously mentioned, ρ is the fluid density, and C is the specific heat per unit mass. With a small Peclet number the heat transport equation simplifies to

$$\frac{\partial T}{\partial t} = \nabla\ T. \tag{2.5}$$

For a steady-state problem like that seen in the CVB we ignore the left-hand side and the equation simplifies to the aforementioned 2D Laplace's equation. The Peclet number is analogous to the Reynolds number discussed in Chapter 4 for the Navier-Stokes momentum equations.

Let us now focus on the case of the heater power of 2.0 W and impose the nondimensional wall temperature value of $T_w = 0.03$. Since the saturation temperature estimated based on measured vapor pressure is about 333 K, this condition corresponds to the characteristic difference of 10 K between the wall and vapor temperatures. To account for non-equilibrium effects during evaporation at the interface, the boundary condition is usually formulated as

$$K\frac{\partial T}{\partial n} + T = 0 \tag{2.6}$$

with $\frac{\partial}{\partial n}$ denoting the normal derivative at the interface and the kinetic parameter defined as

$$K = \frac{kT_s^*}{2\rho_v h^* \mathcal{L}^2}\sqrt{2\pi \bar{R} T_s^*}. \tag{2.7}$$

Here k is the thermal conductivity of pentane, ρ_v the vapor density, $\mathcal{L}$ the latent heat of evaporation, $\bar{R}$ the ideal gas constant per unit mass, and h^* the distance from the corner

to the contact line. Using the value of K from Table 2, the internal heat transfer coefficient estimated based on the 2D model ends up being significantly higher than any of the values discussed in the previous section. The origin of the discrepancy can be explained as follows. Due to very small values of K, the liquid-vapor interface temperature is very close to T_s^*. Then, with the fixed wall temperature, the heat flux, proportional to the temperature difference divided by the layer thickness, is very large. However, in reality localized cooling of the substrate will happen near the contact line. This effect is especially pronounced for the case of zero contact angle considered here, based on the wetting properties of pentane, but is still present for non-zero contact angles. Following the same approach as in our previous study, [8], we build on the study done by Oron at al. [36] and account for such local cooling by using a modified boundary formulation at the solid wall,

$$K_s \frac{\partial T}{\partial n} + T = T_w. \tag{2.8}$$

We consider small values of K_s so that the first term is only significant in the region close to the contact line, i.e. where the liquid layer thickness is small and the heat flux is large. Away from that region, equation (2.8) reduces to the condition of fixed temperature, T_w, taken here to be 0.03. Thus, introduction of the parameter K_s allows us to avoid physically unrealistic heat fluxes near the contact line. Figure 2.6a illustrates the effect of changes in K_s through the nondimensional flux profile along the interface, parametrized by the angle θ with $\theta = 0$ corresponding to $x = 0$, for three different values of K_s. The evaporative flux can be expressed as the normal derivative of temperature T implying mass flux leaving the interface as

$$J = -\frac{\partial T}{\partial n}. \tag{2.9}$$

While all three curves show similar behavior away from the contact lines, there is an order of magnitude difference in the local flux predictions near $\theta = 0$ and $\pi/2$. These higher values of evaporative flux are expected near the contact line where the meniscus is thinner allowing for higher temperatures and therefore higher evaporation.

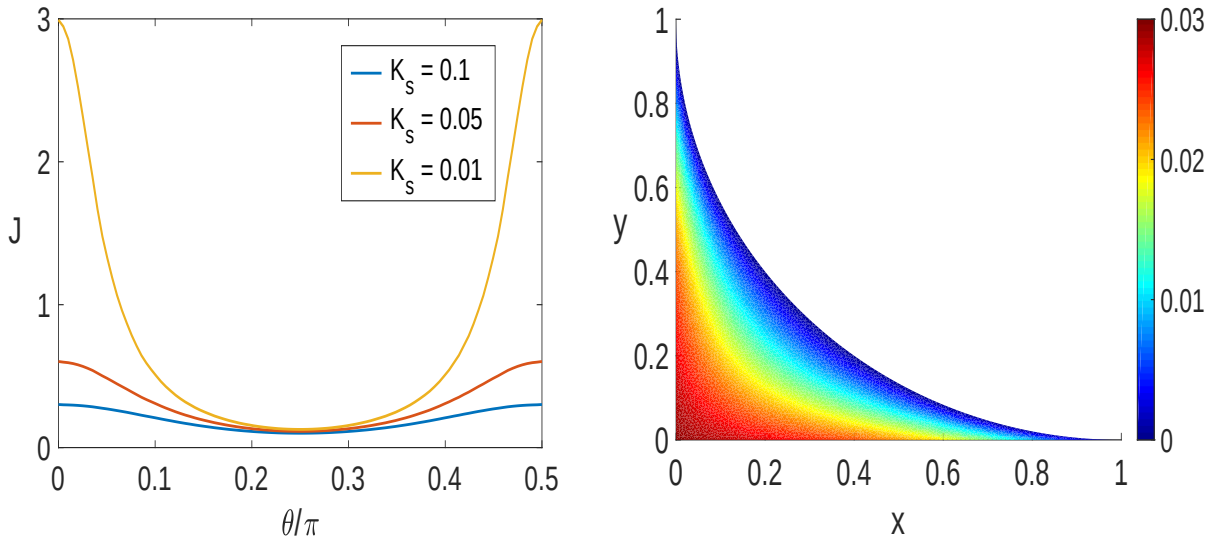

(a) (b)

Figure 2.6: (a) Nondimensional flux profiles at the liquid-vapor interface for varying coefficient K_s and heater power of 2.0W. (b) Nondimensional plot of the temperature in the liquid for $K_s = 0.07$.

The solutions were obtained using finite-element discretization of equation (2.3) as implemented in Matlab's PDE toolbox [31]. The geometry was formed in dimensionless quantities for simplicity. Circle C1 centered at the point (1,1) of radius 1 is subtracted from the square S1 of length and width 1 to create the 2 dimensional wedge with zero contact angle displayed in Figure 2.6b. Matlab allows for specifying coefficents to the general partial differential equation

$$m\frac{\partial^2 u}{\partial t^2} + d\frac{\partial u}{\partial t} - \nabla \cdot (c\nabla u) + au = f \tag{2.10}$$

with either simple Dirichlet or a generalized Neumann boundary condition of the form

$$\mathbf{n} \cdot (c\nabla u) + qu = g. \tag{2.11}$$

We then specified equation (2.3) by setting $c = 1$ and setting the forcing term f and the remaining coefficients to zero. The boundary conditions are specified on "edges," in this case the walls of the cuvette or the interface. To specify the boundary conditions according to

equations (2.8) and (2.6), at the interface a Neumann boundary condition is specified with $q = 1/k$ and $g = 0$, while at the cuvette walls similarly a Neumann condition is specified with $q = 1/K_s$ and $g = T_w/K_s$. The solution is then interpolated along the circular interface via the relation $x = 1 - \cos\theta$ and $y = 1 - \sin\theta$ for θ between 0 and 2π. The flux is integrated using MATLAB's trapezoidal numerical integration routine.

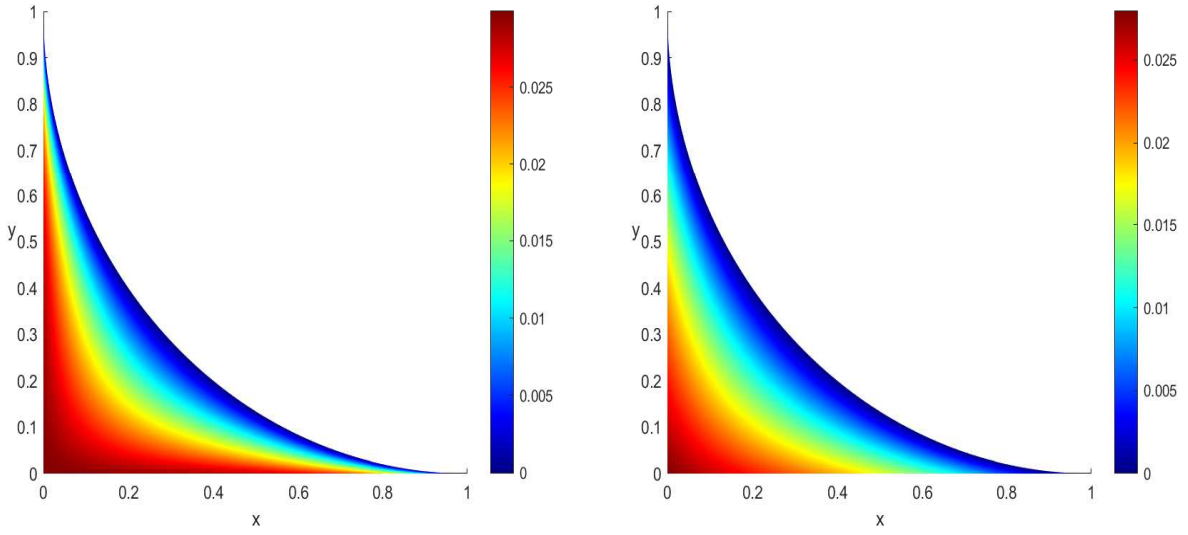

(a) (b)

Figure 2.7: (a) Nondimensional plot of the temperature in the liquid for $K_s = 0.01$ (b) Nondimensional plot of the temperature in the liquid for $K_s = 0.1$.

Figures 2.7 (a-b) illustrate further the effects of utilizing the parameter K_s to model localized cooling in the substrate. The 2D temperature profiles show consistency with the evaporative flux profiles in Figure 2.6a, with lower values of K_s corresponding to higher temperature values near the contact line. The localized cooling is most notable at the contact line where for higher values of K_s the temperature in the liquid displays more uniformity. In contrast eliminating the localized cooling from the model results in higher temperatures near the contact line and although this is expected as Figure 2.6a illustrates that without the localized cooling the evaporative flux can be observed to reach physically unrealistic values without the altered boundary condition including the localized cooling.

We continue the thermal study by observing that the majority of energy loss is used in the process of phase change via evaporation. Once the heat flux profile $J(\theta)$ is found, it can be integrated over the liquid-vapor interface to determine total heat loss in each corner, thus providing an estimate of the internal heat transfer coefficient h_i discussed previously

$$h_i = \frac{4k}{p_i T_w} \int_0^{\pi/2} \frac{\partial T}{\partial n} d\theta. \tag{2.12}$$

We found that $K_s = 0.07$ gives the value of h_i consistent with the estimate obtained in section 2.1. Temperature distribution in the corner obtained for this value of K_s is shown in Figure 2.6b. The wall temperature reduction near the contact line as a result of evaporative cooling is clearly seen; the liquid-vapor interface temperature is close to zero everywhere. Note that the dimensional temperature T^* approaches the saturation temperature T_s^* at the interface as the nondimensional temperature approaches zero.

2.3. Axial heat flux variation and 3D modeling

The average heat flux magnitude in each cross-section, q, is defined as the integral of the flux over the liquid-vapor interface divided by the interface length and can be expressed as

$$q = -\frac{2kT_s^*}{\pi h^*} \int_0^{\pi/2} \frac{\partial T}{\partial n} d\theta. \tag{2.13}$$

The flux varies in the axial direction since the wall temperature is a function of z. Figure 2.8 is obtained from the internal heat transfer term of equation (2.1). The average flux is noticeably higher in the region with higher temperature. The liquid in section II in Figure 1.3 maintains a constant geometry despite the evaporative mass loss. Clearly, liquid flow in the corner is needed to maintain the steady configuration, as discussed in the next section.

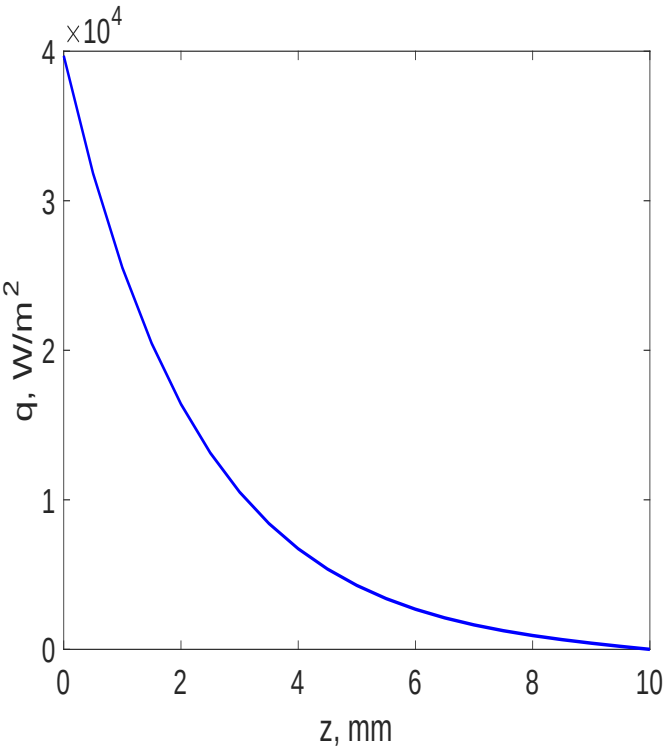

Figure 2.8: Average heat flux as a function of axial coordinate.

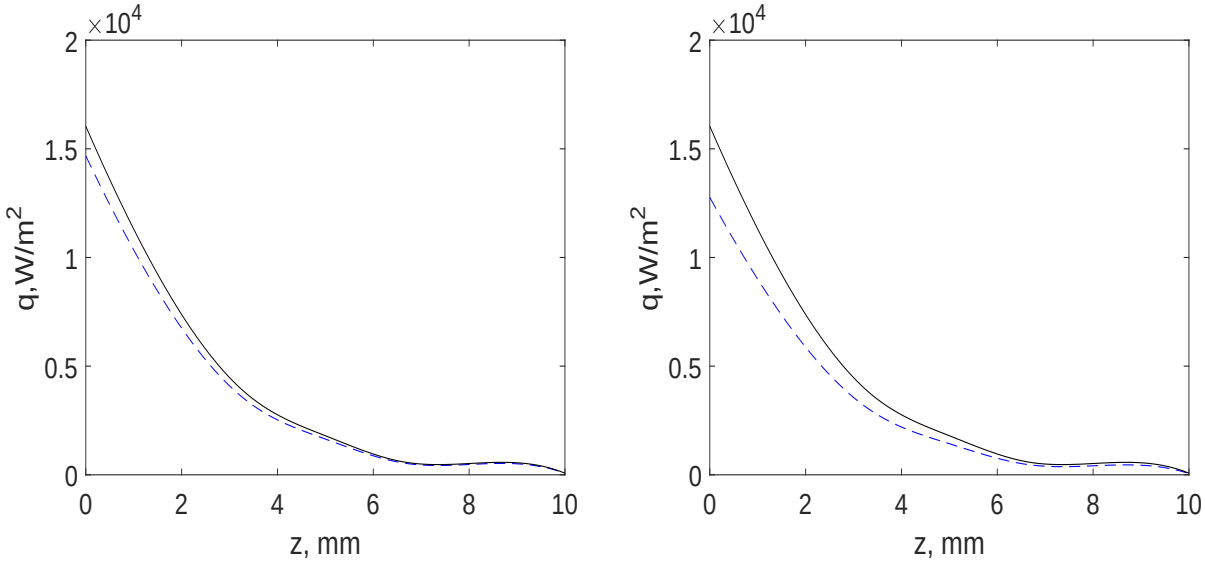

Figure 2.9: (a) Axial heat flux with varying localized cooling parameter $K_s = 0.1, 0.07$. (b) Axial heat flux with varying kinetic parameter $K = 0.01, 10^{-5}$.

In Figures 2.9 (a-b) we compare the changes in the average heat flux due to a change in the localized cooling parameter K_s and the kinetic parameter K using equation (2.13). In both plots the solid black line represents the parameter values associated with matching the experimental data from the CVB experiment, namely $K_s = 0.07$ and $K = 1.7\text{x}10^{-5}$. It's apparent that the the localized cooling has a greater effect on the heat flux as it took a difference three orders of magnitude to get a similar adjustment to the flux as a difference of 0.03 from K_s.

While the results based on 2D heat transfer are more accurate than those based on 1D models, the experimental configuration is clearly three-dimensional. For a better representation of heat transfer within the cuvette we considered a 3D model of the cuvette structure using Matlab's PDE Toolbox [31] in concert with creating a 3D geometry in a CAD program. The numerical approach is similar to that described in the 2D heat transfer, however, boundary conditions are defined on faces instead of edges. The geometry is that of an open-ended cuvette on both the heated end and the cooled end to allow designation of boundary conditions on the interior. The geometry with numbered faces is pictured in Figure 2.10.

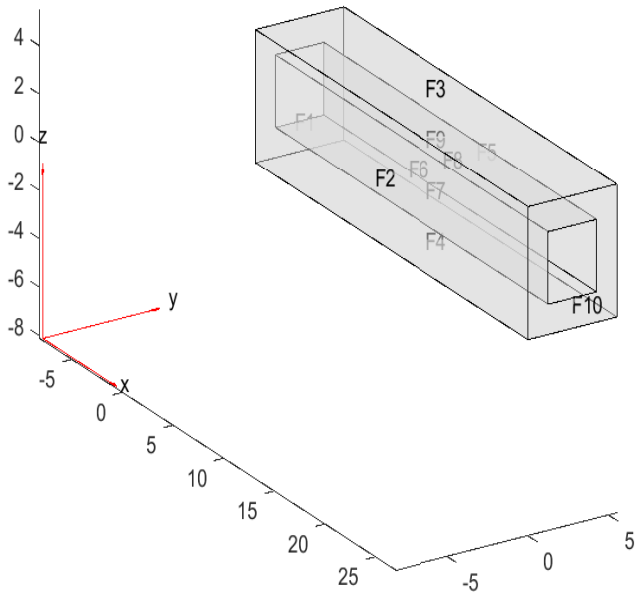

Figure 2.10: 3D geometry of empty cuvette with faces numbered for reference.

The boundary conditions that produce Figure 2.11 are that of a constant temperature at the heated end and cooled-end as described by the experimental results obtained by Chatterjee et al. [11]. The external wall boundaries are defined by zero heat flux and the internal wall boundaries are characterized by a variable internal heat transfer coefficient, for now assumed to be a function of z only. Based on the discussion in the previous subsection, we use the corresponding value for $0 < z < 16$ mm, twice that value between 16 and 21 mm, and zero for the rest of the cuvette. Figure 2.11b illustrates excellent agreement between the 3D model and the experimental data.

Note that now we do not need to introduce an additional adjustable parameter K_s to account for finite conductivity of the substrate as the heat conduction in the substrate is described fully by the three-dimensional model. We also modified the model to account for spatially non-uniform heat loss along the internal wall, representing a more realistic situation when heat loss is significantly higher at the parts of the cuvette covered by the liquid according to the position of contact lines at $h^* = 0.7$ mm from the corners; the result

is shown in Figure 2.12. The middle part of the wall not covered by liquid is characterized by zero heat loss coefficient and thus higher temperature there is seen than in the corners of the same cross-section.

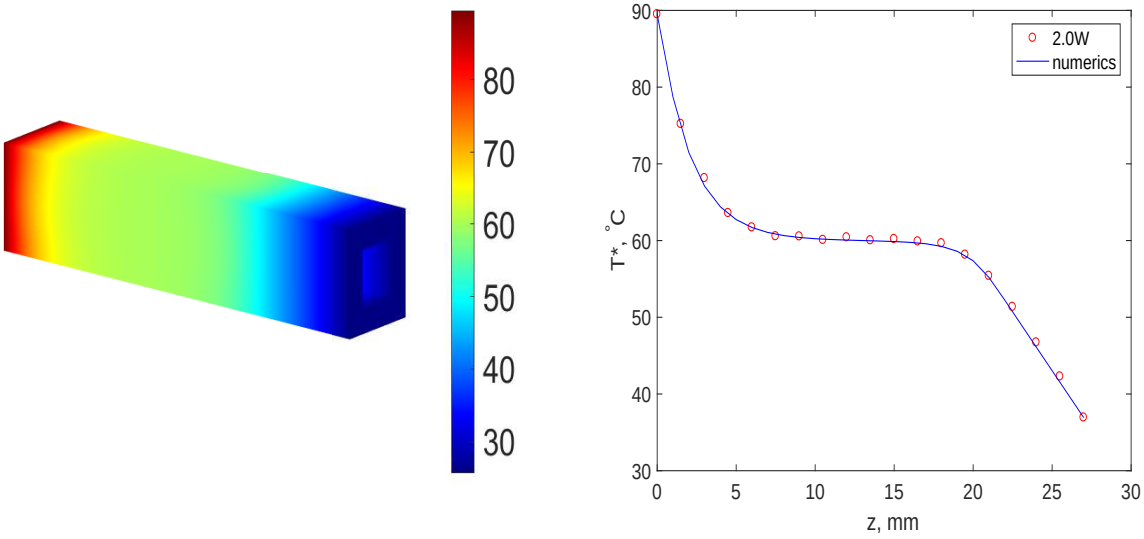

(a) (b)

Figure 2.11: (a) Three dimensional visualization of the heat transfer observed in the quartz cuvette. (b) Comparison of three dimensional model to experimental data.

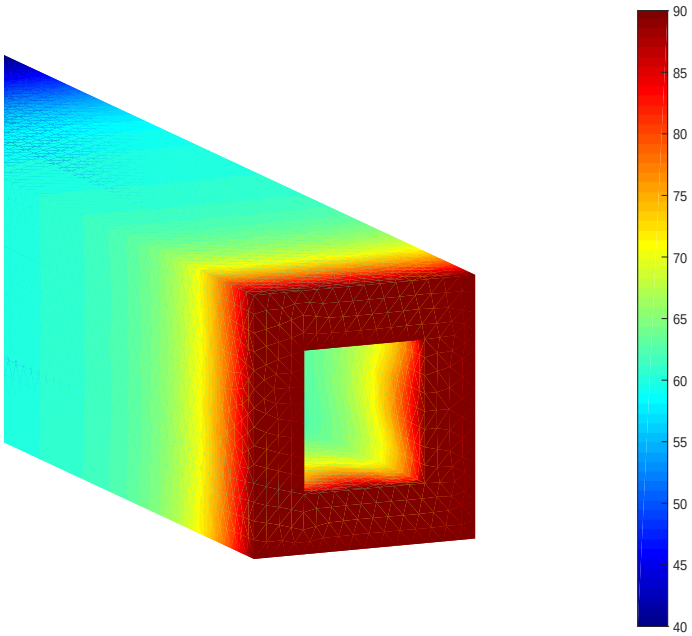

Figure 2.12: Numerical 3D solution near the hot end for the model which accounts for spatial cross-sectional variation of the heat loss coefficient at the inner wall.

Chapter 3

FLUID FLOW IN THE CORNER

3.1. Average axial flow velocity from Navier-Stokes

We now turn our attention to the fluid flow. We assume the liquid to be incompressible and the flow to be governed by the steady dimensional Navier-Stokes and continuity equations,

$$\mathbf{u} \cdot \nabla \mathbf{u} = -\frac{1}{\rho} \nabla p + \nu \nabla^2 \mathbf{u} \tag{3.1}$$

$$\nabla \cdot \mathbf{u} = 0, \tag{3.2}$$

formulated for the domain of the shape illustrated in Figure 2.5; here ν is the kinematic viscosity, p is pressure. The standard no-slip and no-penetration conditions are assumed at the solid boundaries, while the velocity at the evaporating interface is set by the local evaporation rate. The numerical solution of the flow equations is certainly feasible, but is beyond the scope of the present work. Instead, we focus on evaluating flow characteristics based solely on the previously obtained description of heat transfer in the liquid and the condition of conservation of mass. Specifically, integrating equation (3.2) over the cross-sectional liquid phase domain, of the area A_l, leads to

$$\int_{A_l} \left(\frac{\partial u}{\partial x^*} + \frac{\partial v}{\partial y^*} \right) dA + A_l \frac{\bar{w}}{dz} = 0. \tag{3.3}$$

Here we introduce the average axial flow velocity, $\bar{w}$. The integral on the left-hand side of equation (3.3) above can be expressed in terms of integral of the normal flow velocity over the liquid-vapor interface, which in turn matches evaporative mass loss, given by $0.5\pi h^* q/\mathcal{L}$. Thus, the data for average heat flux, e.g. shown in Figure 2.8, can be used to determine $\bar{w}$

without directly solving the flow equations. Combining equation (2.13) and equation (3.3), we find

$$\frac{d\bar{w}}{dz} = -\frac{kT_s^*}{A_l \mathcal{L} \rho} \int_0^{\pi/2} \frac{\partial T}{\partial n} d\theta. \tag{3.4}$$

We now integrate this equation with the condition $\bar{w}(0) = 0$, reflecting the fact that liquid cannot escape since the heated end of the cuvette is sealed. Strictly speaking, the wedge-flow model breaks down before the end of the cuvette is reached, so our approach gives a lower bound of velocity; accounting for evaporation in the flooded region near the heater is likely to increase the estimated velocity. The result of integration can be expressed as

$$\bar{w} = \frac{kT_s^*}{A_l \mathcal{L} \rho} \int_0^z \int_0^{\pi/2} \frac{\partial T}{\partial n} d\theta ds. \tag{3.5}$$

Using numerically obtained temperature profiles and applying quadrature rules to evaluate the integrals in this equation, we obtain the solid line in Figure 3.1. Alternatively, the average heat flux q can be evaluated based on the 1D model, resulting in

$$q = \frac{h_i (T_w^* - T_s^*) p_i}{2\pi h^*}. \tag{3.6}$$

The temperature difference can be estimated from the 1D model, equation (2.1), by assuming that the internal heat loss is the dominant heat transfer mechanism, leading to

$$(T_w^* - T_s^*) = (T_H^* - T_s^*) \exp\left[-\left(\frac{h_i p_i}{k_q A_q} \right)^{1/2} z \right], \tag{3.7}$$

where T_H^* is the temperature at the heated end. This then leads to the analytical formula,

$$\bar{w} = \frac{h_i (T_H^* - T_s^*)}{4 A_l \rho \mathcal{L}} \left(\frac{h_i p_i}{k_q A_q} \right)^{-1/2} \left(1 - \exp\left[-\left(\frac{h_i p_i}{k_q A_q} \right)^{1/2} z \right] \right) \tag{3.8}$$

represented by the dashed line in Figure 3.1, clearly in very good agreement with the predictions of the more complicated numerical model.

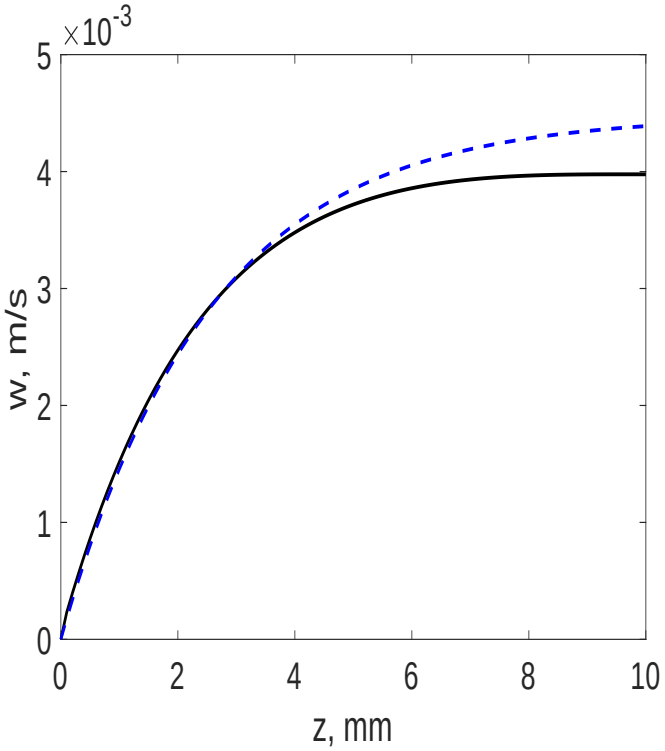

Figure 3.1: Average axial velocity w estimated from evaporative mass loss according to equation (3.5) (solid line) and equation (3.8) (dashed line).

Typical values are on the order of 10^{-3} m/s, which is consistent with the rough estimate of the characteristic velocity,

$$U = \frac{k(T_H^* - T_s^*)}{\rho h^* \mathcal{L}}. \tag{3.9}$$

The discrepancy has to do with the fact that simple estimates of velocity can only be accurate for normal component of the flow velocity at the interface; axial value $\bar{w}$ is expected to be higher since the cross-sectional area is much smaller than the area from which evaporation is taking place. We also note that the result from equation (3.8) suggests an analytical estimate for the maximum axial flow velocity

$$\bar{w} = \frac{h_i(T_H^* - T_s^*)}{4A_l \rho \mathcal{L}} \left(\frac{h_i p_i}{k_q A_q} \right)^{-1/2} \tag{3.10}$$

This estimate, now verified by the numerics, is useful for comparing different regimes of CVB operation. For example, it shows that flow velocity increases linearly with the

temperature difference between the heated end and the saturation value.

For completeness, we now consider the effects of varying the parameters on the boundary conditions on the estimated axial flow velocity by varying K_s and K. In both plots the solid black line refers to the parameter value that matches with the experimental data from the CVB, namely $K_s = 0.07$ and $K = 1.7\text{x}10^{-5}$. From Figures 3.2 (a-b) an increase in values of K_s and K results in a decrease in average velocity. This is in line with the findings from the temperature profiles. As a decrease in K_s resulted in higher evaporation and therefore axial flow. The opposite would be true as seen here. It is also apparent as seen with the average axial heat flux that it take a large change in the kinetic parameter K to result in a similar change to the heat profiles as compared to the localized cooling parameter. Since the approximation for axial velocity is based on the integral of the evaporative flux as is the average axial heat flux we expect changes to be similar.

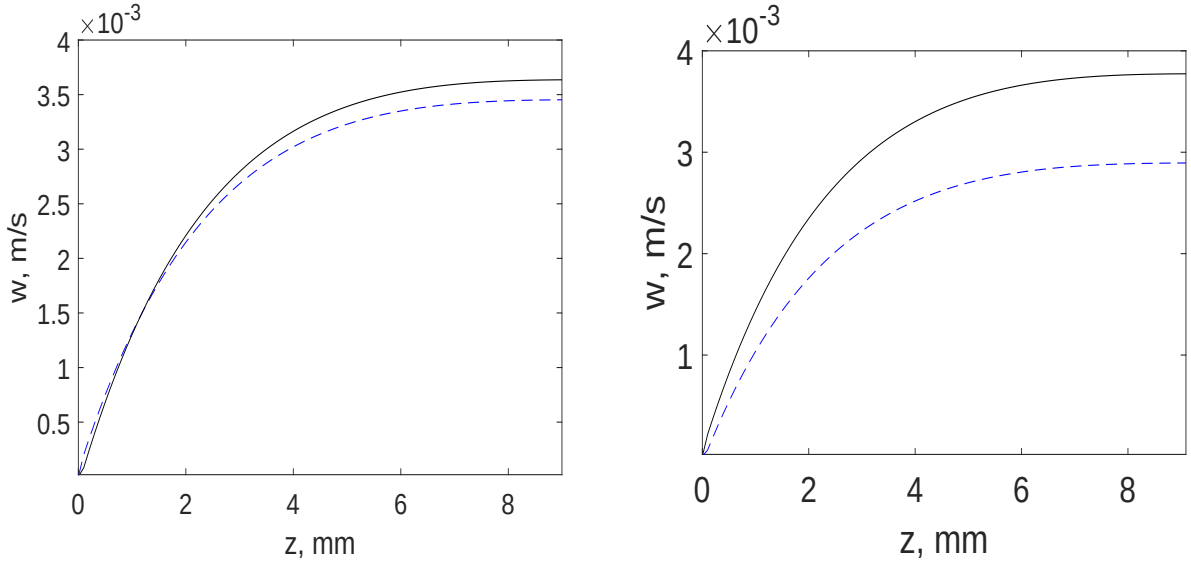

Figure 3.2: (a) Average axial velocity with varying kinetic parameter $K = 0.01, 10^{-5}$. (b) Average axial velocity with varying localized cooling parameter $K_s = 0.1, 0.07$.

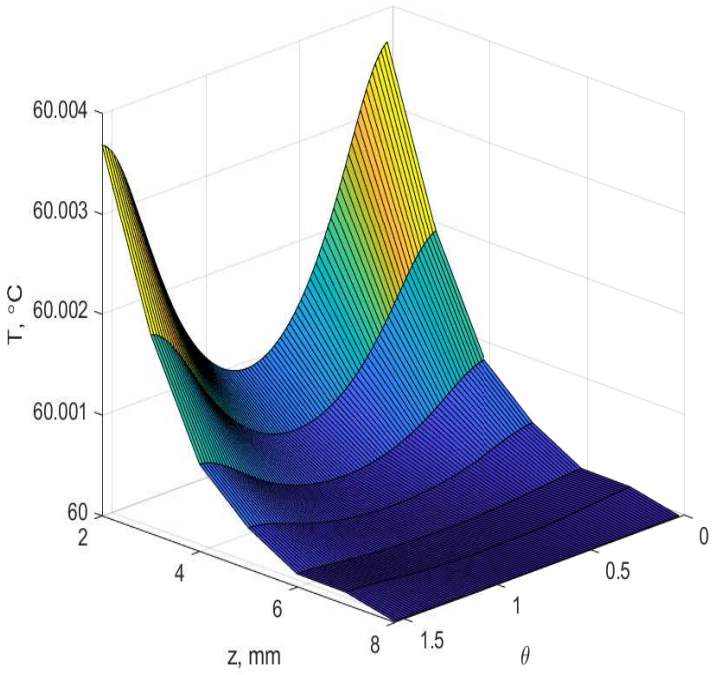

Figure 3.3: 3D plot of surface temperature for section 2 of the CVB displaying the minimal change in surface temperature.

3.2. Discussion of Marangoni flow

Due to the geometry being nearly unchanged, as suggested by Figure 1.3, in the axial direction we believe that capillary forces due to curvature variation are not likely to be the driving force behind changes in axial velocity. An alternative mechanism affecting the flow is provided by Marangoni stresses, as suggested in several previous studies [25, 24, 11]. Since the liquid-vapor interface temperature is now determined from the solution of the 2D heat transfer problem, we are in position to estimate the significance of Marangoni stresses, assuming the surface tension to change linearly with the temperature difference in the form

$$\sigma = \sigma_0 - \gamma(T^* - T_s^*). \tag{3.11}$$

We note that the temperature at the liquid-vapor interface deviates from the saturation value due to non-equilibrium effects, as measured by the constant K. We found that the most significant departures of temperature from the saturation value are seen near the contact line, so we record how the scaled temperature changes along the contact line in Figure 3.4. When expressed in dimensional terms, the temperature gradient turns out to be ~ 2 K/m. We can obtain a rough estimate for the flow due to surface tension change via the relation derived in e.g. Ajaev [2] as

$$\Delta \bar{w} = \frac{\gamma h^*}{2\mu} \left| \frac{dT^*}{dz} \right|. \tag{3.12}$$

This gives a contribution to velocity due to Marangoni stresses on the order of 10^{-4} m/s in the axial direction, which is significantly less than the change in velocity seen in the region near the heater. For further indication of the small temperature gradient in this region Figure 3.3 displays the small surface temperature change. This is valuable added information, as there is little experimental data on the internal temperature of the fluid in the CVB. Thus, while Marangoni effect can contribute to the slow-down of the flow seen near the heated end, other factors are likely to play a role as well, indicating a need for further investigations.

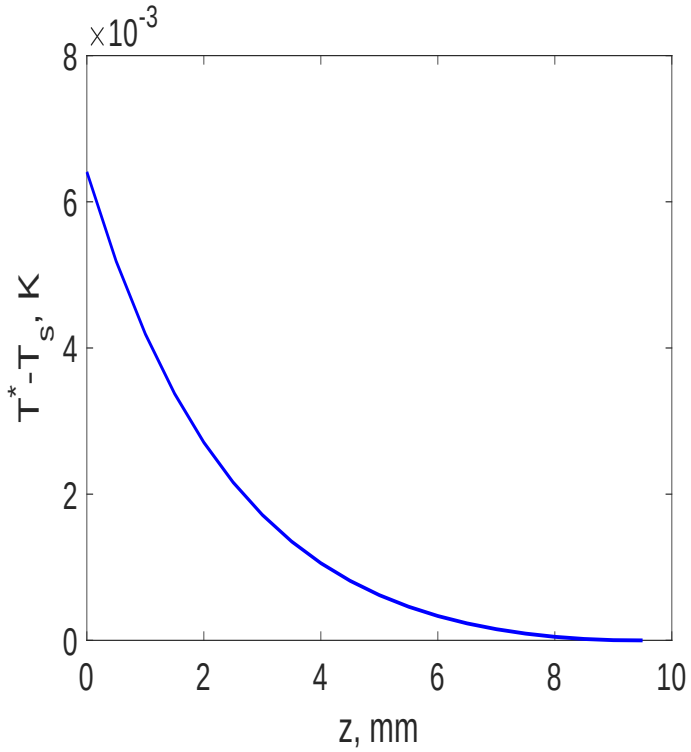

Figure 3.4: Vapor-liquid surface temperature near the contact line as a function of axial coordinate.

Due to the complexity of the problem an accurate 1- or 2-dimensional analysis of the flow is difficult. A 2D cross sectional flow analysis such as that done by Markos et al.[30] gives valuable contributions to our understanding of flow rate within the wedge, but does not take a focused approach on the mass loss due to evaporation at the contact lines. A 2D analysis is limited in that boundary conditions can only be applied at the walls and interface. Typical flow conditions involve no-slip at the walls and evaporation at the interface, however without being able to apply a condition for fluid flux into the domain to replace the fluid lost due to evaporation the models will not adequately describe the flow. We therefore propose that for further investigation a 3D model of one of the wedges from region 2 from Figure 1.3 using the flow approximations obtained from our 2D heat transfer analysis. The interface therefore should allow for fluid flux out of the interface higher in the contact line regions as illustrated in Figure 2.6a and in accordance with the flow described in Figure 3.1 to allow flow into and out of the domain.

3.3. Conclusions

A one dimensional and two dimensional heat transfer solution is presented for the CVB system. In which a variable internal heat transfer coefficient is presented. Fitting the experimental data from [11] to the 1D heat transfer model in the region near the hot end leads to an estimate of the internal heat transfer coefficient of 400 W/(m^2 K) there. However, the heat transfer coefficient is found to increase in the condensation zone near the middle of the cuvette, an observation explained by increased liquid-vapor interface area. Finally, near the cold end the heat transfer is dominated by axial conduction in the liquid phase that fills most of the cross-section and the heat transfer coefficient drops to zero. In the 2D cross-sectional model for temperature the evaporative flux is calculated by taking into account heat transfer in the liquid phase in the corners of the cuvette and introducing a localized cooling parameter into the boundary conditions at the cuvette walls. Heat flux at the liquid-vapor interface is determined and used to estimate the evaporative loss and thus the axial velocity of the flow, with typical average axial flow velocity found to be of the order of 1 mm/s. An analytical estimate of flow velocity is obtained and is shown to be consistent with the numerical results. Effects of 3D heat conduction in the cuvette and the Marangoni stresses are also studied. Further investigation is needed to fully understand the mechanisms of the flow slow-down in the evaporation region.

Chapter 4

EVAPORATION OF DROPLETS

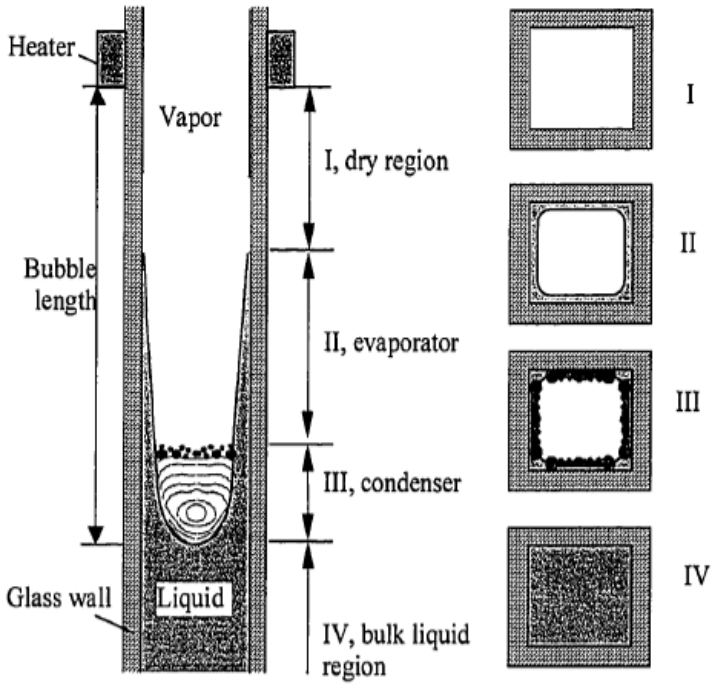

Figure 4.1: Sketch of CVB with emphasis on droplets occuring in cross-section III[51].

The purpose of the present chapter is to develop a model that can reproduce similar results to those observed by Gokhale et al. [19], specifically with a focus on evaporation of observed sessile droplets forming on the walls of the cuvette containing the liquid and vapor as observed in figure 4.1 with the center drop described in Chapter 1. Herein, we derive a one-sided lubrication type model for the moving interface of the droplets observed in the constrained vapor bubble system taking into account surface tension, evaporation, and London van der Waals disjoining pressure. This model uses a one-sided lubrication approach formulated by Burelbach et al. [9], which assumes that the relevant physics occur

in the liquid rather than the vapor as the viscosity, thermal conductivity, and density of the vapor phase are small compared to those of the liquid. To allow for more flexibility in modeling of substrate wetting properties we include a second exponential term to disjoining pressure in the form

$$\Pi(h) = -\frac{\alpha}{h^3} + d_1 \exp\Big(- \frac{h}{d_2} \Big) \tag{4.1}$$

where h is the nondimentional film thickness and α is the scaled Hamaker constant. The exponential term in the disjoining pressure is often used in modeling electrostatic effects in thin films as a result of interaction between ions in the liquid and charges in the substrate, with d_1 and d_2 corresponding to the electric Weber number and the characteristic Debye length respectively. Both terms are defined more precisely in the next section.

There have been many aproaches to mathematically modeling disjoining pressure with early contributions to the topic by Derjaguin [16]. While the originally proposed mechanism of disjoining pressure had to do with unbalanced London van der Waals interactions in thin layers, as measured by the Hamaker constant, later studies incorporated a number of other physical effects, such as interaction of electrical double layer formes near interfaces in aqueous solutions as well as structural forces. To compare as closely as possible to the observations made by Gokhale et al.[19], we use similar physical quantities focusing on n-butanol as the fluid. The key parameters used in this model to match with these experiments are temperature, localized cooling of the substrate defined by K_s, and the two dimensionless values d_1 and d_2 associated with the aforementioned exponential term in the disjoining pressure.

While contact lines in the presence of evaporation have been investigated for decades[33, 15], the models often focus on parametric studies of different regimes and not on describing any particular sets of experimental data. In the present study, we overcome this shortcoming by considering a geometric configuration and conditions which correspond to a specific experimental work, thus allowing us to make the direct connection between the numerical and experimental works under the conditions relevant for a specific application in microgravity similarly done by authors in the journal Microgravity Science and Technology such as Zhang

et al. [50] and Savino et al. [43] with their comparisons of numerics with experiments on evaporating droplets under microgravity conditions.

4.1. Formulation

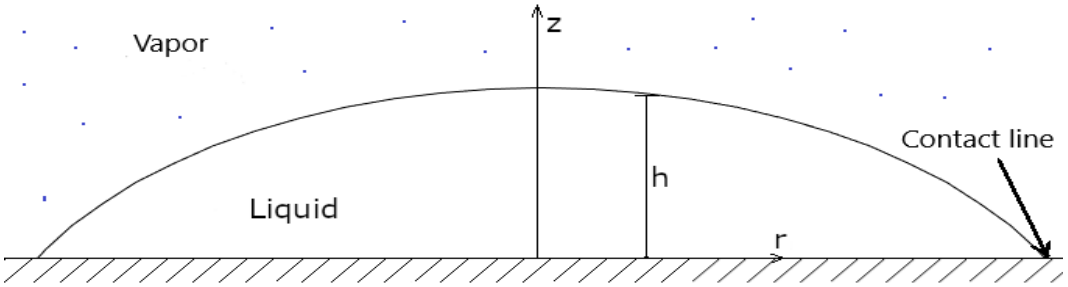

Figure 4.2: Sketch of an axisymmetric droplet.

We wish first to derive a model to simulate the evaporation of an axisymmetric liquid droplet of density ρ and viscosity μ on a uniformly heated substrate in a pure vapor environment as seen in figure 4.2. We will use a lubrication-type approach, common in studies of thin films and droplets [37, 14, 34, 1, 2], and the one-sided model formulated by Burelbach et al. [9].

We begin by defining relevant non-dimensional variables. Similar to the scaling used by Ajaev[1], we define the characteristic radial velocity scale by

$$U = \frac{kT_S^*}{\rho \mathcal{L} R_0}. \tag{4.2}$$

Here k is the thermal conductivity of the liquid, $\mathcal{L}$ is the latent heat of vaporization per unit mass, and R_0 is the initial radius of the base of the droplet, and T_S^* is the equilibrium saturation temperature. Due to the axisymmetric nature of the droplet we ignore the theta terms. We then define the scaling for the remaining variables. To do so, we introduce the characteristic length scales L_z and L_r to scale the vertical z^* and the radial lengths r^* and h^* respectively. The time t^* is scaled by L_r/U and the pressure p^* is expressed in terms of the surface tension σ and the curvature $\frac{\partial^2 h^*}{\partial r^{*2}}$ is scaled by $\sigma L_z/L_r^2$. Finally we make use of the difference in length scales namely that L_z is much smaller than L_r to define the small quantity $\epsilon = L_z/L_r$. With ϵ defined we scale the vertical velocity w^* by ϵU, since we expect the impact of the radial velocity to be much larger than the vertical velocity. This choice is

essential for keeping both terms in the continuity equation.

Now consider the radial momentum equation of the Navier-Stokes equations

$$\frac{\partial u^*}{\partial t^*} + u^*\frac{\partial u^*}{\partial r^*} + w^*\frac{\partial u^*}{\partial z^*} = -\frac{1}{\rho}\frac{\partial p^*}{\partial r^*} + \frac{\mu}{\rho}\left(\frac{1}{r^*}\frac{\partial}{\partial r^*}\left(r^*\frac{\partial u^*}{\partial r^*}\right) + \frac{\partial^2 u^*}{\partial z^{*2}} - \frac{u^*}{r^{*2}}\right). \tag{4.3}$$

Using the aforementioned scalings the scaled momentum equation becomes

$$\frac{U^2}{L_r}\left(\frac{\partial u}{\partial t} + u\frac{\partial u}{\partial r}\right) + \frac{\epsilon U^2}{L_z}w\frac{\partial u}{\partial z} = -\frac{\sigma L_z}{\rho L_r^3}\frac{\partial p}{\partial r} + \frac{\mu U}{\rho L_r^2}\left(\frac{1}{r}\frac{\partial}{\partial r}\left(r\frac{\partial u}{\partial r}\right) + \frac{L_r^2}{L_z^2}\frac{\partial^2 u}{\partial z^2} - \frac{u}{r^2}\right). \tag{4.4}$$

We then divide by $\frac{U\mu}{\rho L_r L_z}$ to produce the Reynolds number $\frac{\rho L_r U}{\mu}$ on the left hand side.

$$\frac{\rho L_r U}{\mu}\left(\frac{\partial u}{\partial t} + u\frac{\partial u}{\partial r}\right) + \frac{\rho L_z \epsilon U}{\mu}w\frac{\partial u}{\partial z} = -\frac{\sigma}{U\mu}\epsilon^2\frac{\partial p}{\partial r} + \frac{\epsilon}{r}\frac{\partial}{\partial r}\left(r\frac{\partial u}{\partial r}\right) + \frac{L_r}{L_z}\frac{\partial^2 u}{\partial z^2} - \epsilon\frac{u}{r^2} \tag{4.5}$$

Assuming small Reynolds number we remove the left hand side and eliminate any order ϵ terms resulting after division by $\frac{L_r}{L_z}$ in

$$\frac{\sigma}{U\mu}\epsilon^3\frac{\partial p}{\partial r} = \frac{\partial^2 u}{\partial z^2}. \tag{4.6}$$

We now introduce the capillary number using the terms in front of the pressure gradient according to

$$\mathrm{Ca} = \frac{\mu U}{\sigma}. \tag{4.7}$$

The capillary number for most flows in small scale systems is very small, on the order of $10^{-5} - 10^{-6}$, so it can clearly be treated as a small parameter in our derivation. Then to maintain the pressure gradient as an order 1 term in our asymptotic development we define the characteristic length scales $L_r = R_0$ and $L_z = R_0\mathrm{Ca}^{1/3}$ so that the capillary number is small enough to balance the ε^3 term. Finally, the pressure scale becomes $\sigma\mathrm{Ca}^{1/3}/R_0$. The equation in θ is neglected due to the assumption of the droplet being axisymmetric. A similar

derivation can be followed for the vertical momentum equation and the continuity equation of the cylindrical Navier-Stokes equations to produce three of the four governing equations

$$\frac{\partial^2 u}{\partial z^2} = \frac{\partial p}{\partial r}, \tag{4.8}$$

$$\frac{\partial p}{\partial z} = 0, \tag{4.9}$$

$$\frac{\partial u}{\partial r} + \frac{u}{r} + \frac{\partial v}{\partial z} = 0, \tag{4.10}$$

$$\frac{\partial^2 T}{\partial z^2} = 0. \tag{4.11}$$

We use u and v as the velocity components in the radial and vertical directions respectively with their aforementioned scales. The fourth equation here is obtained by applying the scaling procedure defined above to the energy equation, with the assumption that the Peclet number is an order one quantity. The non-dimensional temperature T is defined in terms of the dimensional one, T^*, according to

$$T = \frac{T^* - T_S^*}{\mathrm{Ca}^{2/3} T_S^*}. \tag{4.12}$$

Equations (4.8) through (4.11) make up the non-dimensional governing equations in our model. We now continue to the interfacial boundary conditions. We first introduce the evaporative mass flux J scaled by $\rho U \mathrm{Ca}^{1/3}$ for use in the kinematic boundary condition and interfacial energy balance

$$J + u\frac{\partial h}{\partial r} - v = \frac{\partial h}{\partial t}, \tag{4.13}$$

$$J = -\frac{\partial T}{\partial z}. \tag{4.14}$$

Equation (4.13) relates the local fluid flow with the evaporative flux to determine the change in film thickness h over time. This condition is central to providing a time component to the evolution equation for film thickness. While equation (4.14) relates the evaporative flux to the temperature gradient, and nicely illustrates with the negative sign the relationship

between temperature leaving the system and mass flow leaving as well due to evaporation. The normal stress condition at the interface includes contributions from capillarity and disjoining pressure as follows.

$$p - p_v = -\frac{\partial^2 h}{\partial r^2} - \frac{1}{r}\frac{\partial h}{\partial r} - \frac{\alpha}{h^3} + d_1 \exp\Big(-\frac{h}{d_2}\Big). \tag{4.15}$$

Here we introduce the two term disjoining pressure. The first term is inversely proportional to the cube of the film thickness and contains the order one parameter α defined by $|A|/(\sigma_0 R_0^2 \mathrm{Ca})$, A being the Hamaker constant. For modeling purposes the second term gives greater control over the contact angle of the evaporating droplet for better agreement with the observed experiments [3]. We note that disjoining pressure becomes important when the film thickness becomes very thin near the apparent contact line. This form of the disjoining pressure can lead to a singularity as h approaches zero. This is addressed by the inclusion of the adsorbed film as mentioned previously.

The dynamics of liquid-vapor interfaces can be affected by the thermocapillary effect, as discussed e.g. in [29, 1], but this effect is not expected to be strong for microscale droplets observed by Gokhale et al. [19], so we neglect it here.

Suppose p_v is the nondimensional vapor pressure which is assumed to be constant in this one-sided approach. The scaled interfacial temperature T^i is related to the local mass flux and pressure jump at the interface through the non-equilibrium condition[4, 1], which takes the form

$$KJ = \delta(p - p_v) + T^i, \tag{4.16}$$

where

$$K = \frac{\rho U \sqrt{2\pi \bar{R} T_S^*}}{2\rho_v \mathcal{L} \mathrm{Ca}^{1/3}}, \qquad \delta = \frac{\sigma_0}{\mathcal{L}\rho R_0 \mathrm{Ca}^{1/3}}. \tag{4.17}$$

Here $\bar{R}$ is the gas constant per unit mass. The parameters K and δ measure the importance of kinetic effects and deviations from the equilibrium pressure in the liquid, respectively. Derivation of the formula for K is based on the kinetic gas theory while δ is found from

equilibrium thermodynamics.

4.2. Evolution equation

We now seek to solve the re-scaled system of governing equations and boundary conditions. We begin by solving equation (4.9) via integration, which gives us a formula for the pressure p as:

$$p = p_1, \tag{4.18}$$

where p_1 is a function of r only. Due to this dependence for pressure on the radial component only, integrating the momentum equation (4.8) twice and applying the no slip condition, namely $u = 0$ at $z = 0$ and zero shear stress condition, $\frac{du}{dz} = 0$ at $z = h$, at the interface we obtain the lubrication-type velocity profile:

$$u = \frac{1}{2}\frac{\partial p_1}{\partial r}(z^2 - 2zh). \tag{4.19}$$

Next substituting equation (4.19) into the kinematic condition (4.13) combined with the integral form of the conservation equation gives

$$\frac{\partial h}{\partial t} + J = \frac{1}{3r}\frac{\partial}{\partial r}\left[rh^3\frac{\partial p_1}{\partial r}\right]. \tag{4.20}$$

We now move to the scaled flux J. We use the non-equilibrium equation (4.16) with the relation of the scaled interfacial temperature T_i to the heater temperature T_0 and the mass-flux J via $T_i = T_0 - Jh - K_sJ$. Here we follow the approach of Oron et al. [37] and introduce the thermal resistance of the layer of quartz separating the heater and the liquid similar to that done in Chapter 2 with the localized cooling of the substrate. Based on the parameters of the experiments of Gokhale et al. [19], we use an order of magnitude estimate $K_s \approx 10$. This gives an equation after substitution of the pressure jump for the mass-flux in the form

$$J = \frac{T_0 - \delta\left(\frac{\partial^2 h}{\partial r^2} + \frac{1}{r}\frac{\partial h}{\partial r} + \frac{\alpha}{h^3} - d_1\exp\left(-\frac{h}{d_2}\right)\right)}{K + K_s + h}. \tag{4.21}$$

Substituting this equation into equation (4.20), leads to a differential equation for the film thickness h(r,t):

$$\begin{aligned} 0 =& \frac{\partial h}{\partial t} - \frac{\delta\left[\frac{\partial^2 h}{\partial r^2} + \frac{1}{r}\frac{\partial h}{\partial r} + \frac{\alpha}{h^3} - d_1 \exp\left(-\frac{h}{d_2}\right)\right] - T_0}{K + K_s + h} \\ &+ \frac{1}{3r}\frac{\partial}{\partial r}\left[r h^3 \frac{\partial}{\partial r}\left(\frac{\partial^2 h}{\partial r^2} + \frac{1}{r}\frac{\partial h}{\partial r} + \frac{\alpha}{h^3} - d_1 \exp\left(-\frac{h}{d_2}\right)\right)\right]. \end{aligned} \tag{4.22}$$

Equation (4.22) is the focus of the numerical results found in the study. It was solved numerically using finite-difference discretization for spatial derivatives and time stepping with the DVODE package [20]. The time step is $\Delta T = 5$, and the same start-up procedure is used as in Ajaev [1]. The scaled time t used in the plots below is measured from the time when the droplet radius is equal to unity. The parameter values are determined by the conditions of the experiment of Gokhale et al. [19], as shown in Table 4.1. The heater temperature is not measured in experiments, but it is stated that the superheat is small, a statement also supported by our simulations. In comparison with experiments below, we use rescaled superheat ΔT such that $T_0 = 0.001\Delta T$. One can interpret ΔT as the dimensional superheat divided by its actual characteristic value based on experiments rather than being scaled by a quantity proportional to the saturation temperature. More details on the numerics are contained in Chapter 5 which details a more complicated version of this model. More details are given on the initial condition, boundary conditions, and numerical considerations in Chapter 5. A similar model is developed with a more complex form of the disjoining pressure, so we felt it more instructive to be covered there.

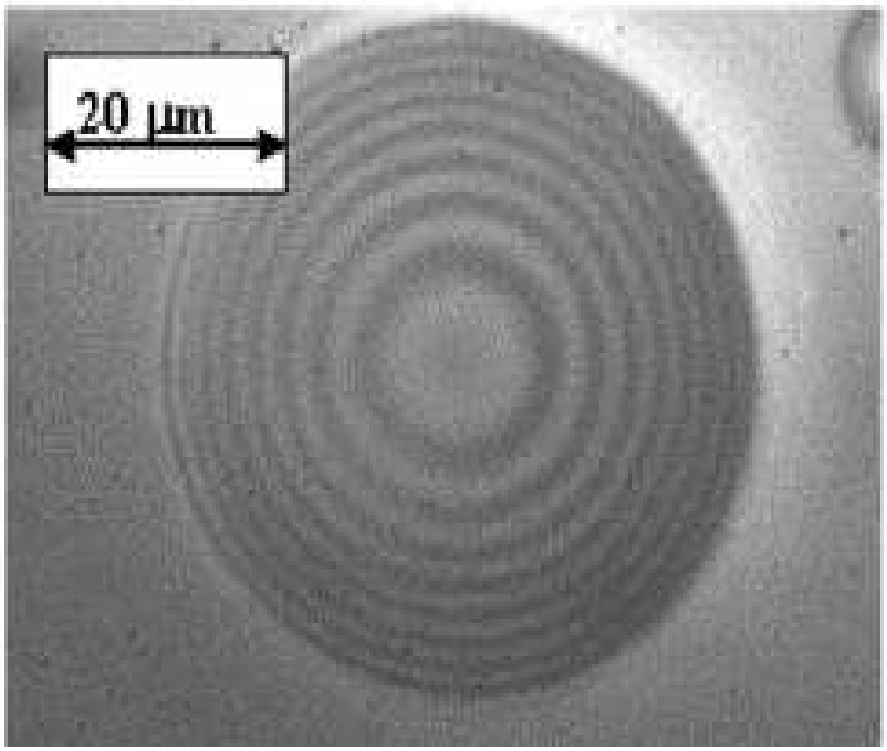

Figure 4.3: Photo of droplets observed in the experiments by Gokhale et al. [19].

Some comments should be mentioned on the choice of droplet size. In Gokhale et al. [19] images are presented of droplets measuring 20 μm as seen in figure 4.3. The experimental data present in figure 4.7a below recorded a radius of curvature slightly higher than 4x10^{-4} meters on a droplet with a contact angle of 4.6 degrees. As illustrated in figure 4.4 a simple geometric argument of assuming the droplet to be approximately the same shape as a spherical cap provides the following relationship between the radius of curvature and the wetting radius.

$$r = R\sin\theta \tag{4.23}$$

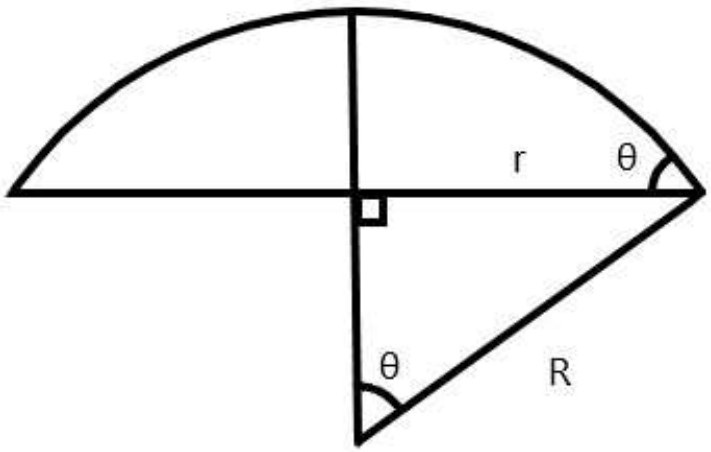

Figure 4.4: Sketch of a spherical cap for determining relationship between the radius of curvature R and the wetting radius r.

Here θ is the contact angle, R the radius of curvature, and r the wetting radius of the droplet. Equation (4.23) gives the relation that for a droplet of radius of curvature 4×10^{-4} m and a contact angle $\theta = 4.6$ degrees the wetting radius of the corresponding droplet should be approximately one order of magnitude smaller. Thus the choice of initial wetting radius of 50 μm was made to start the numerical results slightly above the observed experimental results for matching with the radius of curvature measured by the experimentalists.

Table 4.1: Parameter values for n-butanol

Thermal conductivity	$k = 0.15$ W m^{-1}K^{-1}[27]
Saturation temperature	$T_S^* = 318.15$ K [19]
Density	$\rho = 810$ kg/m^3[19]
Latent heat of vaporization	$\mathcal{L} = 591{,}300$ J/kg[19]
Radius	$R_0 = 50$ μm[19]
Viscosity	$\mu = 0.00137$ Pa s[27]
Vapor density	$\rho_v = 2.85$ kg/m^3[38]
Surface tension at saturation temperature	$\sigma_0 = 0.0254$ N/m^2[19]
Velocity	$U = 2.00$ x 10^{-3} m/s
Capillary number	Ca $= 1.08$ x 10^{-4}
Kinetic Parameter from eqn. (4.17)	$K = 6.32$
Thermodynamic parameter from eqn. (4.17)	$\delta = 2.23$ x 10^{-5}
Scaled Hamaker constant	$\alpha = 1.46$ x 10^{-9}

4.3. Results and discussion

The numerical simulations produce interface shapes such as the one seen in figure 4.5 illustrating the evaporation of the droplets over time. Clearly, the droplet has nearly constant curvature away from the contact line, but the interface rapidly changes shape in the contact line region, eventually transitioning to a flat adsorbed film. More discussion on the adsorbed film is featured in Chapter 5 under section Numerical considerations.

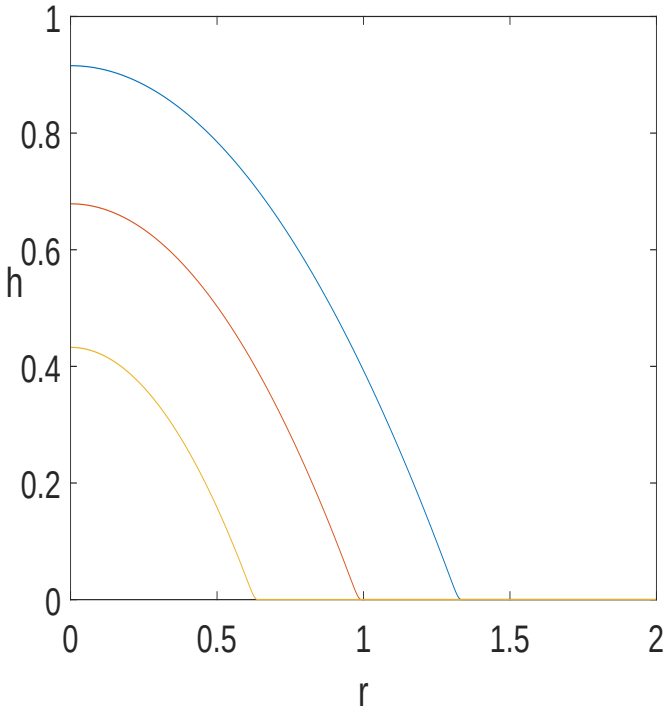

Figure 4.5: Snapshots of the interface shape recorded from the numerical simulation in nondimensional coordinates at times $t = 60, 360$, and 660 respectively.

The rate of change of the interface shape during evaporation strongly depends on the evaporative mass loss. The profile of the evaporative flux is shown in figure 4.6. There is clearly an increase in the vicinity of the contact line, but not as dramatic as was reported in several well-known studies of droplets and menisci [1, 39, 35]. This can be explained in part by the small value of the droplet thickness; however, the introduction of thermal resistance in the quartz layer or localized cooling as introduced earlier contributes the most to the shape of the evaporative flux. In Chapter 2 we showed that introduction of localized cooling

has the effect of decreasing evaporative flux near the contact line. This was essential in this study to match with experiments and to avoid unrealistically high heat fluxes. Another interpretation of this is not that evaporation along the interface has increased, but rather than evaporation near the contact line has decreased. This leads to the smaller spike at the contact line.

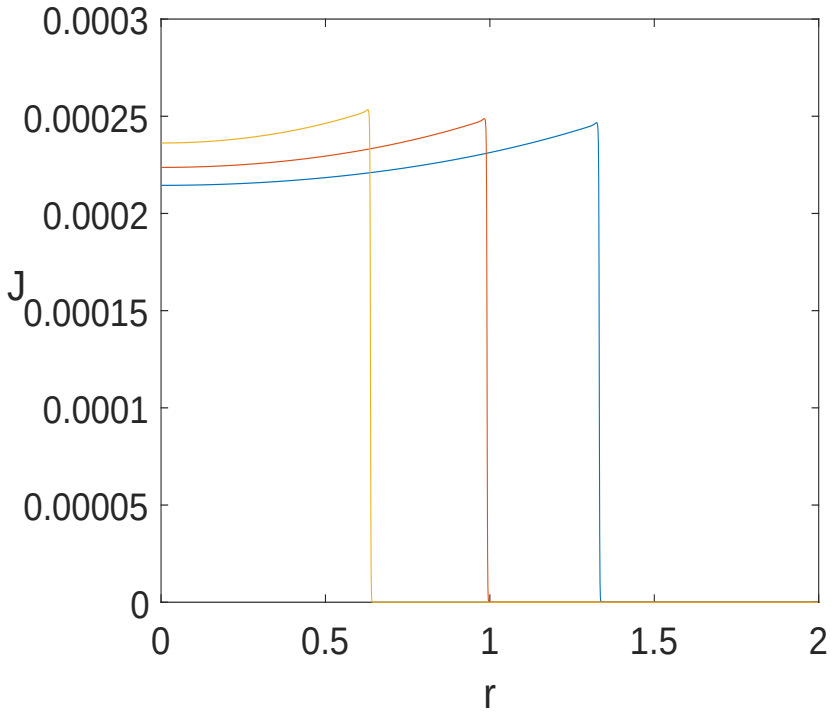

Figure 4.6: Snapshots of the interfacial evaporative flux profile from the numerical simulation at times $t = 60, 360$, and 660 respectively.

For the purposes of comparison with the experimental data, we recast the results in dimensional form and then focus on the time evolution of the radius of curvature at the top of the droplet, the quantity which was studied extensively in the experiments of Gokhale et al. [19]. Numerically, this is done by calculating the curvature via finite differences at the top of the droplet where $r = 0$. The radius of curvature is then defined as the reciprocal of the curvature. This value is then tracked over the duration of evaporation overlayed with the experimental data from Gokhale et al. [19] to produce the plots in figures 4.7

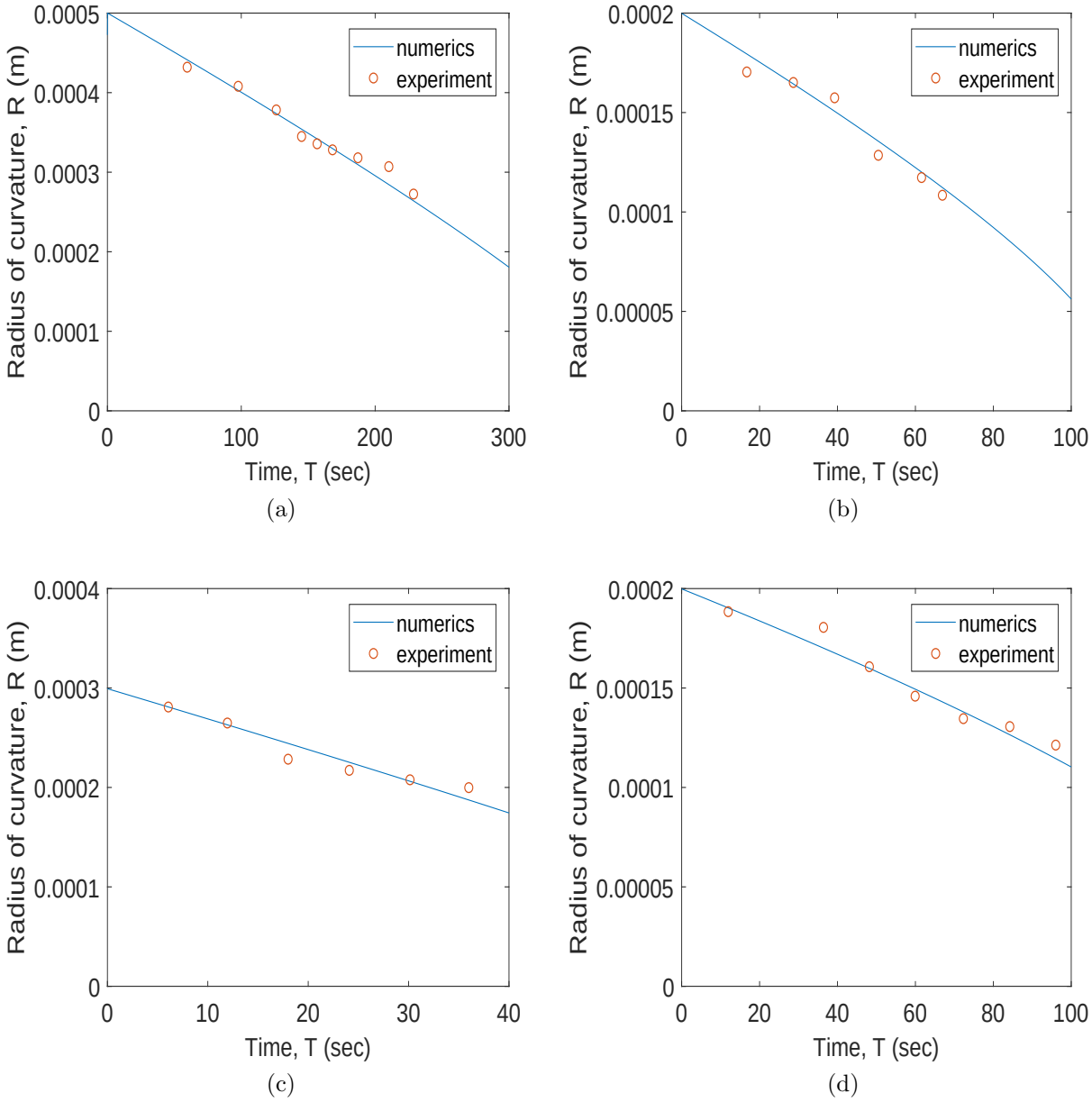

Figure 4.7: Comparison of numerical results with observed experimental data with $d_1 = 100$ and $d_2 = 0.0155$.

Remarkably, after a short transient, the evolution is described by a nearly linear function, as was observed in experiments. The parameter ΔT was used to adjust the rate of change for the evaporation of the droplet. For figures 4.7(a-d) ΔT had values of 0.32, 0.25, 1.16, and 0.07 respectively. The change in substrate temperature can be explained by differing locations of the observed droplets. The parameter d_2 was chosen to get an average contact angle to the droplets reported by Gokhale et al. [19]. Figures 4.7(a-d) were reported to have droplets with contact angles equal to 4.6, 4.4, 4.2, and 3.9 degrees, respectively. The values of d_1 and d_2 provide a contact angle of 4.3 degrees.

4.4. Variation on parameters d_1 and d_2.

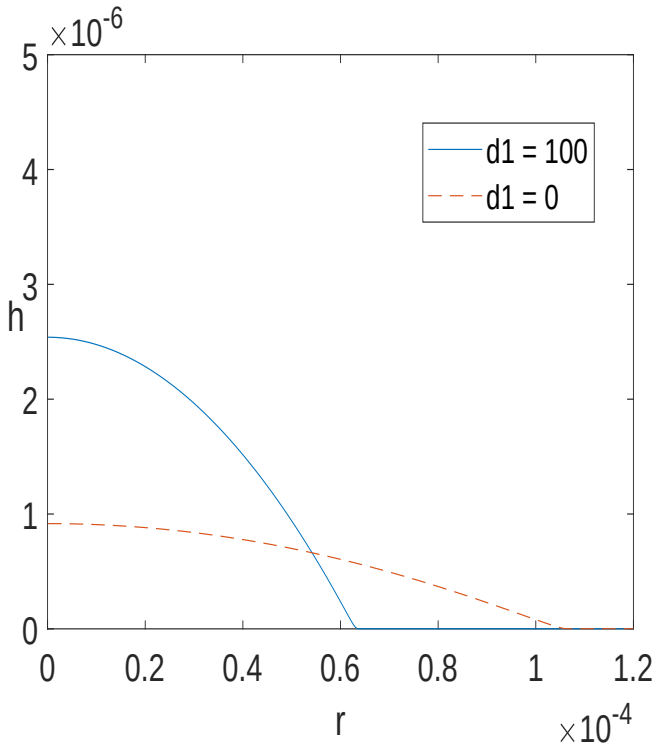

Figure 4.8: Dimensional comparisons of contact angle and interfacial shape from the contribution of the second term in disjoining pressure taken at non-dimensional time $t = 60$

To solidify the modeling choice of including the second disjoining pressure term, figure 4.8 illustrates the presence of the aforementioned second term. The contact angle change is drastic with the absence of the term setting the parameter d_1 to zero resulted in a nearly

zero contact angle of 0.85 degrees. Addition of the term gave a contact angle consistent with observed measurements of 4.3 degrees. Furthermore figure 4.9a seems to suggest that addition of this second term gives excellent control over contact angle with the contact angle θ growing monotonically with d_1.

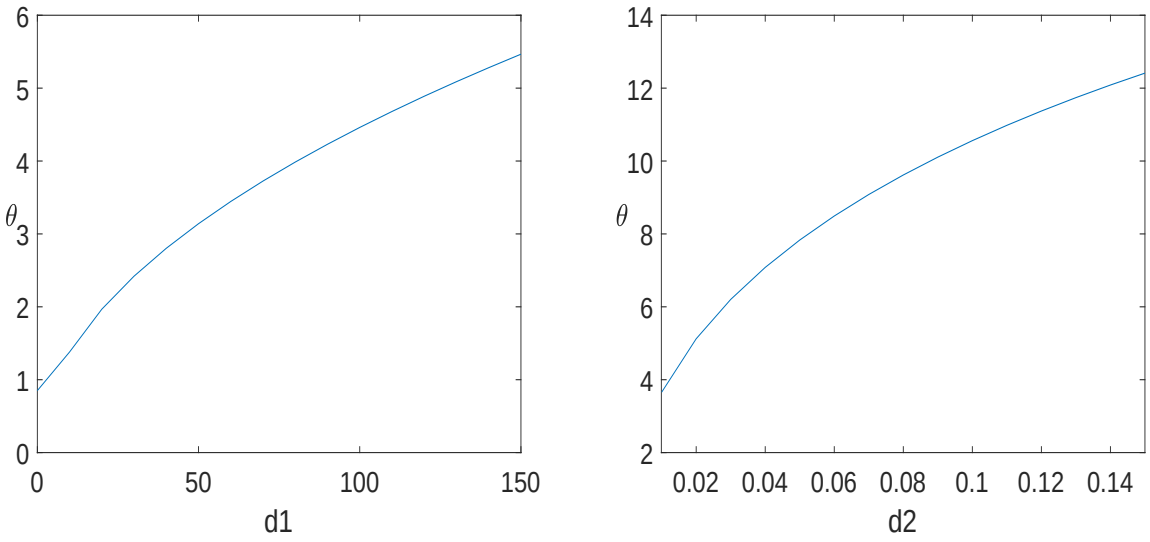

(a) (b)

Figure 4.9: (a) Effect of the parameter d_1 on contact angle. (b) Nondimensional plot of the temperature in the liquid for $K_s = 0.07$.

Similarly d_2 also gives good control over the contact angle with a similar behavior to that of d_1 however with much smaller values. Interestingly enough; however, despite dependence on d_2 the adsorbed film is unaffected by changes in d_2. This is easily understood through analysis on the equation for adsorbed film thickness. More detail is given on the equation for adsorbed film thickness in Chapter 5, but for this section the adsorbed film is the value of h that satisfies the transcendental equation

$$\delta\left(-\frac{\alpha}{h^3} + d_1 \exp\left(-\frac{h}{d_2}\right)\right) + T_0 = 0. \tag{4.24}$$

After some algebra the value of the adsorbed film can be given by the intersection of the two curves defined by the equations

$$F_1(h) = ln\left(\frac{\alpha}{d_1 h^3} - \frac{T_0}{d_1 \delta}\right), \tag{4.25}$$

$$F_2(h) = \frac{-h}{d_2}. \tag{4.26}$$

Equation (4.25) gives a nearly vertical function just right of the origin with equation (4.26) being a line with slope $-1/d_2$. Due to the proximity to the origin a change in slope to a line through the origin does little to the solution of these two equations with the exception of small values of d_2 which produce unrealistic adsorbed film thicknesses. In practice this lack of dependence on d_2 is beneficial as numerically the thickness of the adsorbed film must be calculated each time parameter values are changed. Adjustment of the contact angle can then be realized without adjustment to the adsorbed film by modifying d_2 rather than d_1. The adsorbed film thickness is however, affected by the choice of d_1 with a thicker adsorbed film associated with small values of d_1. Figure 4.10 suggests that for large values of d_1 the adsorbed film thickness reaches an asymptotic limit of 0.5 nm. These findings in concert with figure 4.9a also suggest that small contact angles correspond to thicker adsorbed films.

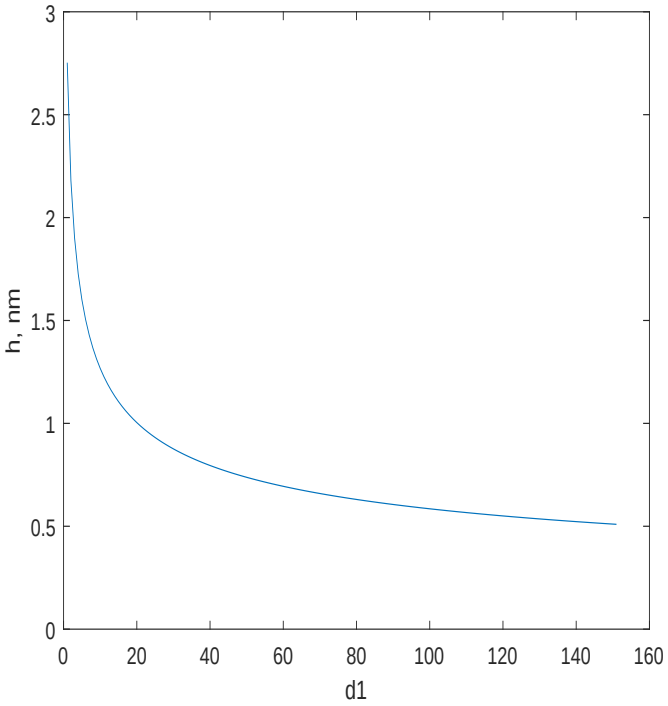

Figure 4.10: Dimensional plot of the effect of the parameter d_1 on the thickness of the adsorbed film .

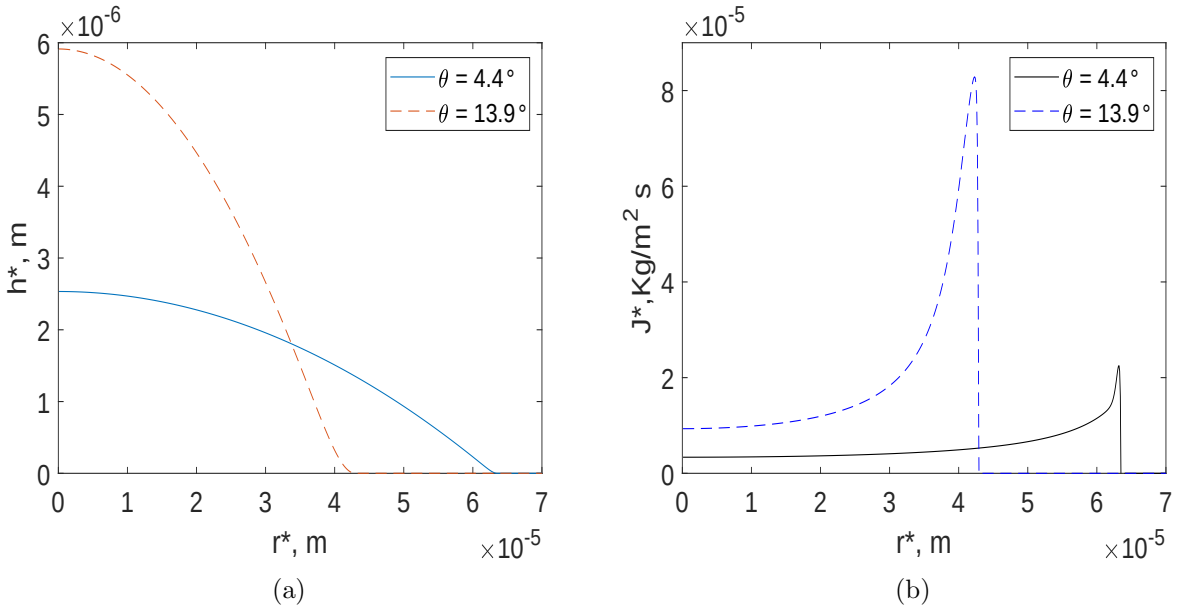

Figure 4.11: (a)Dimensional plot of the change in contact angle to droplet interface shape. (b) Dimensional plot of the evaporative flux due to change in droplet shape.

With the ability to easily define the contact angle by adjusting the parameter d_2 we can consider the effects of contact angle change on droplet interface and evaporative flux profiles. Keeping parameters $K_s = 0.3$ and $d_1 = 100$ we create two droplets with contact angles 4.4 and 13.9 degrees corresponding to a d_2 value of 0.15 and 0.2 respectively. This leads to drastically different interface and evaporative flux profiles as pictured in figure 4.11. The droplet became considerably taller with a larger contact angle, and despite the same value for the localized cooling parameter the evaporative flux is much larger on the droplet with larger contact angle. One thing we learn from this is the influence of curvature on the evaporative flux. Increasing d_2 does little to the value of the second disjoining pressure term, which leads to the main change in evaporative flux being the terms pertaining to curvature. Higher curvature in a droplet seems to correspond to higher values of evaporative flux. This is consistent with evaporation rates predicted by Anderson and Davis [15].

4.5. Variations of the localized cooling parameter

Earlier discussion on the localized cooling parameter K_s have illustrated its effect on the evaporative flux near the contact line. Figure 4.12 further illustrates this with higher values of K_s corresponding to lower evaporative flux. Mathematically, this is expected from the relationship between the interfacial temperature and heater power given earlier. Solving this equation for the mass flux J gives

$$J = \frac{T_0 - T_i}{h + K_s}. \tag{4.27}$$

With constant temperature difference, increasing the value of K_s creates a smaller quantity for J. Figure 4.12 also gives clarity to the evaporative flux profiles seen in figure 4.6. It's apparent from this figure that the evaporative flux stays relatively the same for the length of the droplet until approaching the contact line where the film thickness gets smaller allowing for higher evaporation due to higher temperatures in the fluid. This means that these somewhat irregular flux profiles are due to a smaller flux at the contact line rather than a larger flux along the droplet interface.

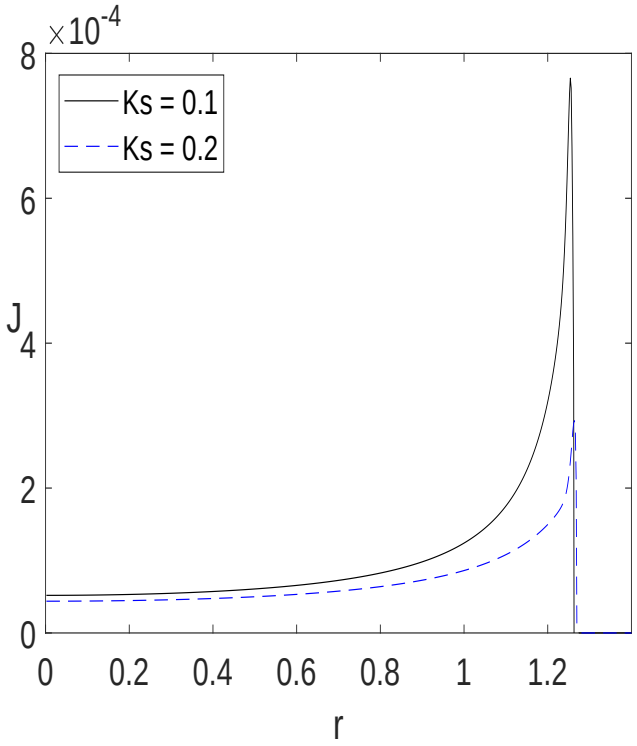

Figure 4.12: Comparison of localized cooling values for K_s on the evaporative flux profile.

Another illustration of the effect of varying K_s directly related to changes in evaporative flux is that of evaporation time. Figure 4.13 shows an almost double time difference in evaporation time for doubling K_s. Comparing this figure to the comparisons made to experiments, the change in curvature over time does not stay linear as the droplet gets closer to evaporation. Though mostly linear, once the droplet reaches a certain size evaporation increases all over the droplet, which rapidly speeds up evaporation.

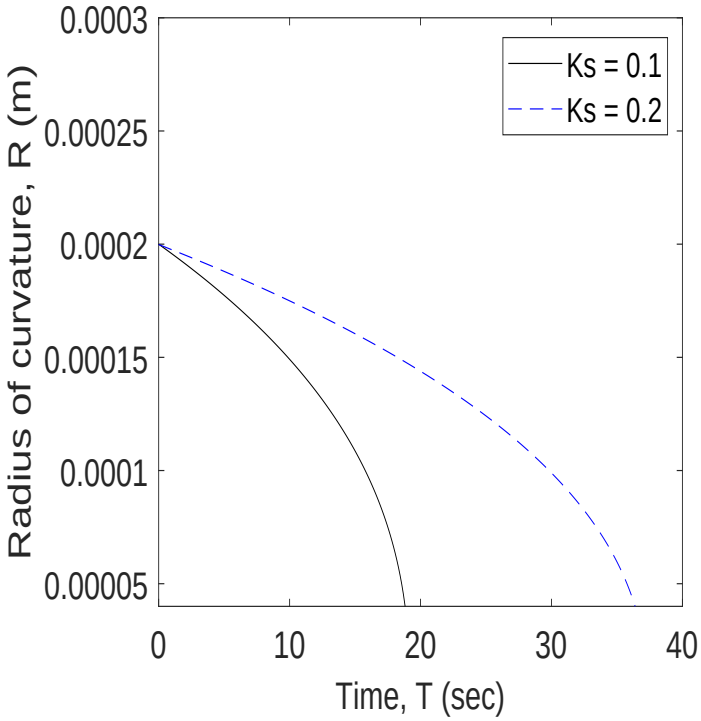

Figure 4.13: Comparison of localized cooling values for K_s on the evaporation rate as determined by decline in the radius of curvature over time.

4.6. Conclusions

We develop a mathematical model of an evaporating droplet observed in the constrained vapor bubble experimental set-up. The motion of receding contact line is described using two-component disjoining pressure coupled with the effects of phase change and capillarity. The results include dynamics of interface shapes during droplet evaporation, including the radius of curvature at the top of the droplet expressed in dimensional form. The evaporative flux is found to increase toward the contact line, but not as sharply as in the case of evaporating meniscus due to the addition of localized cooling of the substrate. Detailed studies of the effect of evaporative cooling parameter K_s on the solutions are conducted. Increase in K_s leads to lower local heat flux near the contact line and thus slower evaporation. Radius of curvature at the top of the droplet is found to decrease in a linear fashion with the slope consistent with experimentally measured values. A second term in the disjoining pressure

gives excellent control over contact angle for matching with experiments or observing different regimes.

Chapter 5

ELECTROSTATIC EFFECTS ON DROPLET EVAPORATION

Liquid on almost any surface is susceptible to contamination and formation of surface charges which can produce electrostatic forces to be present in the liquid as charged ions in the liquid can interact with the surface. We will introduce the effects of electrostatic forces as done by Ketelaar and Ajaev [22] by adding them via the non-linear Poisson-Boltzmann equation. Mazzoco and Wayner [32] suggested that on a quartz surface adding the electrostatic effects could be done through coupling them with the disjoining pressure with the following normal and tangential stress balances

$$\left\|\mathbf{n}\cdot\mathbf{T}^f\cdot\mathbf{n}\right\| = \sigma\nabla\cdot\mathbf{n} + \Pi_{vdw} + \Pi_{el}, \tag{5.1}$$

$$\left\|\mathbf{n}\cdot\mathbf{T}^f\cdot\mathbf{t}\right\| = 0, \tag{5.2}$$

where $\|\cdot\|$ denotes the jump across the interface, $\mathbf{n}$ and $\mathbf{t}$ are the unit normal and tangential vectors at the interface, respectively, and $\mathbf{T}^f$ is the fluid stress tensor. Here Π_{vdw} and Π_{el} are the van der Waals and electrostatic contributions to the disjoining pressure respectively. The van der Waals term was introduced with an alternate approximation to the electrostatic forces in equation (4.1). Ketelaar and Ajaev [22] note that this approach has two limitations. The first is that the formulas for disjoining pressure are valid only for small values of the film thickness h and therefore can't be used to describe the coupling between global changes in the interface shape and changes in the electric field. A model with such coupling would require solving the Poisson-Bolztmann equation. The second is that electrostatic effects are neglected in the tangential stress balance, which can turn out to be important when comparisons with experimental data are conducted. To mitigate the second shortcoming they suggested replacing the fluid stress tensor $\mathbf{T}^f$ with by a more general expression of the

form $\mathbf{T}^f + \mathbf{T}^e$ the second term being the electrostatic (Maxwell) stress tensor

$$\mathbf{T}^e = \varepsilon \left(\mathbf{E}\mathbf{E} - \frac{1}{2}|\mathbf{E}|^2 \mathbf{I} \right), \tag{5.3}$$

where ε is the dielectric permittivity of the liquid, $\mathbf{E}$ is the electric field, and $\mathbf{I}$ is the identity tensor. The Maxwell stress tensor is used to account for the effects of the electric field on induced charge dipoles in the medium, accounted for through ε, and mobile charges, i.e. the ions found in the fluid [41, 26]. Equation (5.3) allows us to rewrite the aforementioned interfacial stress balances as

$$\left\| \mathbf{n} \cdot \mathbf{T}^f \cdot \mathbf{n} \right\| + \frac{1}{2}\varepsilon \left[(\mathbf{E} \cdot \mathbf{n})^2 - (\mathbf{E} \cdot \mathbf{t})^2 \right] = \sigma \nabla \cdot \mathbf{n} + \Pi_{vdw}, \tag{5.4}$$

$$\left\| \mathbf{n} \cdot \mathbf{T}^f \cdot \mathbf{t} \right\| + \varepsilon (\mathbf{E} \cdot \mathbf{n})(\mathbf{E} \cdot \mathbf{t}) = 0. \tag{5.5}$$

To the best of our knowledge, previous works do not incorporate these effects on evaporating droplets in this manner.

5.1. Formulation

We wish now to derive a model to simulate the evaporation of a liquid droplet of density ρ and viscosity μ on a uniformly heated substrate in pure vapor environment. The derivation is very similar to that of the droplet model formulated in Chapter 4, so instead of going through the same steps this section will highlight the differences and refer to equations in Chapter 4 where things remain the same. We first introduce the leading order non-linear Poisson-Boltzmann equation

$$\frac{\partial^2 \psi}{\partial z^2} = \kappa^2 \sinh \psi. \tag{5.6}$$

Here ψ is the electric potential scaled by $\bar{\psi} = k_B T_s^* / e$, with k_B the Boltzmann constant and e the elementary charge. We note that the general nonlinear Poisson-Boltzmann equation is derived from the classical Poisson's equation of electrostatics by assuming that the distribution of ions falls in line with the Boltzmann statistics [23]. The form of equation (5.6) is due

to the assumption of only two types of ions. The ion concentration is typically determined from the solution of the Nernst-Planck equation [23], and requires that ion transport be neglected which is the case for small Peclet number, already established in Chapter 2. Next we introduce an order one quantity $\kappa \equiv R_0 Ca^{1/3}/\lambda_D$ which forms the ratio of the characteristic film thickness to the Debye length λ_D defined at the saturation temperature by

$$\lambda_D = \left(\frac{\varepsilon k_b T_S^*}{2 n_0 e^2} \right)^{1/2}. \tag{5.7}$$

Here n_0 is the ion concentration away from the interface. The Debye length measures thickness of screening layers of charge formed near interfaces. The boundary conditions for equation (5.6) are formulated as

$$\psi(0) = \psi_0, \psi_z(h) = \kappa q. \tag{5.8}$$

Where q is the charge density scaled as

$$q^* = \frac{\varepsilon \bar{\psi} q}{\lambda_D} \tag{5.9}$$

as used in the Grahame equation, [23]. Let us now introduce the electric Weber number as done by Conroy et al. [12] as

$$Q = \frac{\varepsilon \bar{\psi}^2}{\sigma R_0}, \tag{5.10}$$

which we will use to measure the strength of electrostatic effects in our model.

The governing equations with the added electrostatic effects are therefore

$$\frac{\partial^2 u}{\partial z^2} = \frac{\partial}{\partial r} \left(p - \kappa^2 \bar{Q} \cosh \psi - \frac{\alpha}{h^3} \right), \tag{5.11}$$

$$\frac{\partial}{\partial z} \left(p - \kappa^2 \bar{Q} \cosh \psi \right) = 0, \tag{5.12}$$

with the conservation and heat equation remaining the same as those derived in the previous chapter. Since the values of Q tend to be small, we use an order one parameter $\bar{Q} =$

Q/Ca. The scalings on the nondimensional quantities of temperature T and evaporative flux J remain unchanged along with the kinematic boundary condition and interfacial energy balance introduced earlier. The normal stress condition at the interface, however, includes contributions from the electrostatic effects and takes the form:

$$p - p_v = -\frac{\partial^2 h}{\partial r^2} - \frac{1}{r}\frac{\partial h}{\partial r} + \frac{1}{2}\kappa^2 \bar{Q} q^2 - \frac{\alpha}{h^3}. \tag{5.13}$$

Next we introduce the dimensional charge density q^* as used by Ketelaar and Ajaev [22] in the form:

$$q^* = -\varepsilon(\mathbf{E} \cdot \mathbf{n}) \tag{5.14}$$

This is a result of the disparity in dielectric permittivity between the liquid and the vapor phases, the liquid assumed to have a much higher value of ε than the vapor. The value of q^* is assumed to be constant in this study. With the dimensional charge density thus defined with the aforementioned length scales the interfacial stress balances result in the shear stress condition at the interface of the form

$$\frac{\partial u}{\partial z} = -\kappa \bar{Q} q \frac{\partial \psi}{\partial h}\frac{\partial h}{\partial r}. \tag{5.15}$$

The scaled interfacial temperature T^i is related to the local mass flux and pressure jump at the interface through the non-equilibrium condition [4], which including the electrostatic terms takes the form:

$$KJ = \delta\Big(p - p_v - \kappa^2 \bar{Q} \cosh\, \psi\Big) + T^i, \tag{5.16}$$

where K and δ are defined as previously in Chapter 4. A similar derivation to that done for the evolution equation in the previous chapter results in an evaporative flux J of the form:

$$J = \frac{T_0 - \delta\left(\frac{\partial^2 h}{\partial r^2} + \frac{1}{r}\frac{\partial h}{\partial r} - \frac{1}{2}\kappa^2 \bar{Q} q^2 + \kappa^2 \bar{Q} \cosh\, \psi + \frac{\alpha}{h^3}\right)}{K + h}. \tag{5.17}$$

and the evolution equation for the film thickness $h(r,t)$ as

$$\frac{\partial h}{\partial t} - \frac{\delta\left[\frac{\partial^2 h}{\partial r^2} + \frac{1}{r}\frac{\partial h}{\partial r} - \frac{1}{2}\kappa^2\bar{Q}q^2 + \kappa^2\bar{Q}\cosh\psi + \frac{\alpha}{h^3}\right] - T_0}{K+h} + \frac{1}{3r}\frac{\partial}{\partial r}\left[rh^3\frac{\partial}{\partial r}\left(\frac{\partial^2 h}{\partial r^2} + \frac{1}{r}\frac{\partial h}{\partial r} + \kappa^2\bar{Q}\cosh\psi + \frac{\alpha}{h^3}\right)\right] + \frac{1}{2r}\kappa\bar{Q}q\frac{\partial}{\partial r}\left[rh^2\frac{\partial\psi}{\partial h}\frac{\partial h}{\partial r}\right] = 0. \tag{5.18}$$

This equation will be solved numerically, as described in the next section, with the boundary conditions of zero derivatives in the flat adsorbed film and the conditions of symmetry at $r = 0$. Note that we do not include the parameter K_s as done in the previous models. We do this to focus solely on the electrostatic effects to see how they effect interactions between the substrate and the fluid and the evolution of the droplet surface as well as the heat flux.

5.2. Numerical considerations

Let us begin with the initial condition. To avoid the known contact line singularity we make use of what is referred to in the literature as a precursor or adsorbed film. The thickness of the adsorbed film is determined by setting the evaporative flux J as well as the first and second derivatives or h with respect to r equal to zero and solving for h via the transcendental equation

$$h_{ads} = \left[\frac{\delta\alpha}{T_0 + \delta\left(\kappa^2\bar{Q}\cosh\psi - \frac{1}{2}\kappa^2\bar{Q}q^2\right)}\right]^{1/3}, \tag{5.19}$$

since ψ is a function of h, or an alternative simplified approximation,

$$h_{ads} \approx \left(\frac{\delta\alpha}{T_0}\right)^{1/3}, \tag{5.20}$$

valid only when the electrostatic terms can be neglected. We find typical nondimensional thickness for the scaled adsorbed film to be on the order of 10^{-4} or in dimensional terms on the order of tens of nanometers. Having the adsorbed film defined by zero evaporative flux cleverly balances the evaporative flux term to zero on the adsorbed film, so despite the

small film thickness which typically suggests that evaporation is high, the adsorbed film will have zero evaporative flux. This is beneficial in results, because it allows for focus on the dynamics in the evaporating thin film.

Now having defined the adsorbed film, we set the initial condition to be that of an upside down parabola sitting on the adsorbed film, such that the initial thickness $h_0(r)$ is equal to the parabola everywhere the parabola is greater than or equal to the height of the adsorbed film, or more precisely

$$h_0(r) = \begin{cases} \beta - \beta r^2 & h_0(r) \geq h_{ads} \\ h_{ads} & h_0(r) < h_{ads} \end{cases} \tag{5.21}$$

Where β is chosen to best represent the droplet. The initial condition however has little impact on the global evolution of the droplet. Note that there is also a difficulty in getting a precise initial condition in experiments when initially placing the droplet on the substrate.

With the initial condition defined, let us now move to the boundary conditions and discretization. For the axisymetric case, we consider half of the droplet as pictured in the results from figure 4.5 from Chapter 4. Now consider a droplet sitting on an adsorbed film composed of n evenly spaced points consisting of $h_i, i = 1, 2, 3, ..., n$ where $i = 1$ corresponds to the center of the droplet, and $i = n$ corresponds to the end of the domain where the adsorbed film sits. Then for boundary conditions we apply a symmetry condition such that at $i = 1$, $h_{i-1} = h_{i+1}$ and $h_{i-2} = h_{i+2}$. We'll note that at $r = 0$ the concern for a singularity occurs due to the $1/r$ terms in the evolution equation (5.18). These singularities can be addressed by noting that the Taylor expansion at the point for the 1st derivative is

$$\frac{\partial h}{\partial r}(r,t) = \frac{\partial h}{\partial r}(0,t) + r\frac{\partial^2 h}{\partial r^2}(0,t) + r^2\frac{\partial^3 h}{\partial r^3}(0,t) + O(r^3). \tag{5.22}$$

Noting then that at the center of the droplet, corresponding to $r = 0$, where the 1st and 3rd order derivatives vanish this leaves the approximation

$$\frac{1}{r}\frac{\partial h}{\partial r}(r,t) \approx \frac{\partial^2 h}{\partial r^2}(0,t) + O(r^3). \tag{5.23}$$

This substitution eliminates all $1/r$ terms, removing the singularity. At the opposite boundary we similarly apply a condition of zero derivatives; however, the majority of these points should typically be equal to the calculated value of h_{ads}. We use finite difference schemes to evaluate the derivatives, and the DVODE software packeage as referenced in Chapter 4. Backward differencing method is chosen for advancing the solution in time.

For the electrostatic potential we use an approximation of equation (5.6) as

$$\frac{\partial^2 \psi}{\partial z^2} = \kappa^2 \psi \tag{5.24}$$

with the boundary conditions of constant charge density at the liquid surface and constant potential at the substrate. The differential equation can then be solved leading to the profile

$$\psi = \frac{q \sinh \kappa z + \psi_0 \cosh (h\kappa - \kappa z)}{\cosh hk} \tag{5.25}$$

which can be verified to satisfy the boundary conditions given in equation (5.8). The potential can now be evaluated at $z = h$ and the result combined with the evolution equation for the film thickness derived above.

5.3. Preliminary results

The expectation is that the addition of electrostatic effects for droplet evaporation, building on the model resented by Ajaev [1], will provide a more accurate model to match with experiments. The results in Chapter 2 required a second term to the disjoining pressure as well as localized cooling to control the evaporative flux. Preliminary results are promising that introduction of the electrostatic forces will have a similar effect to that of the localized cooling. We found that with an increase to the electric Weber number, and therefore stronger influence of the electrostatic effect, that the evaporative flux decreases near the contact line. Not as substantially as that seen in Chapter 4, but the profile of the evaporative flux matches better with that seen in previous studies with a large increase near the contact line.

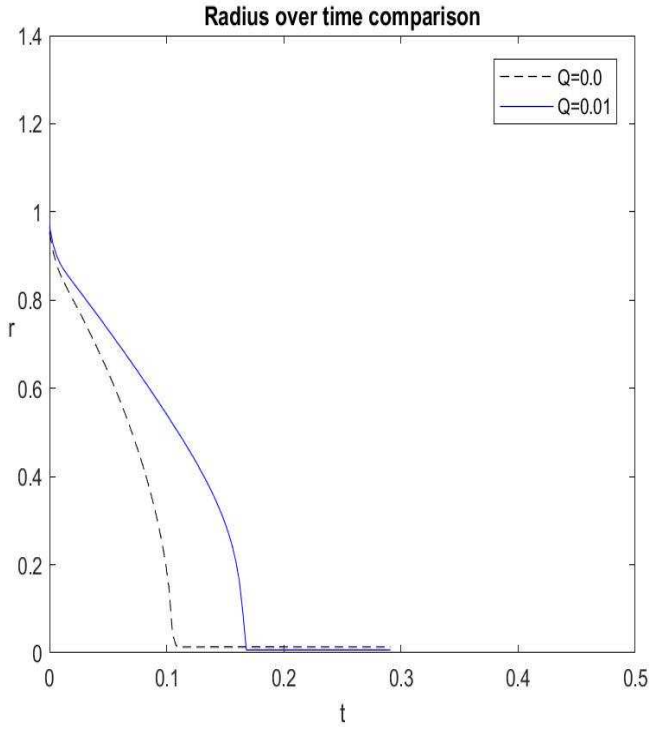

Figure 5.1: Evaporation of droplets observed by the decreasing of radius over time.

Indeed the lower evaporative flux is apparent when considering the radius over time as seen in figure 5.1. Clearly, with the introduction of the electrostatic effects the droplet evaporation slows compared to neglecting the effects in the model. The evaporation itself behaves

similarly to that observed by the droplet model from Chapter 4 with a seemingly linear rate until the droplet reaches a small enough size around 0.2 in nondimensional terms where evaporation is nearly instantaneous. This plot is obtained by allowing the initial condition as stated in the previous subsection to form to evolve to a droplet of non dimensional radius 1. At which point the time is set to zero and the radius is recorded. The radius of the droplet itself is found by scanning the droplet from left to right for the maximum of the curvature, which is where the contact line is located. The droplet is then allowed to run its course to complete evaporation.

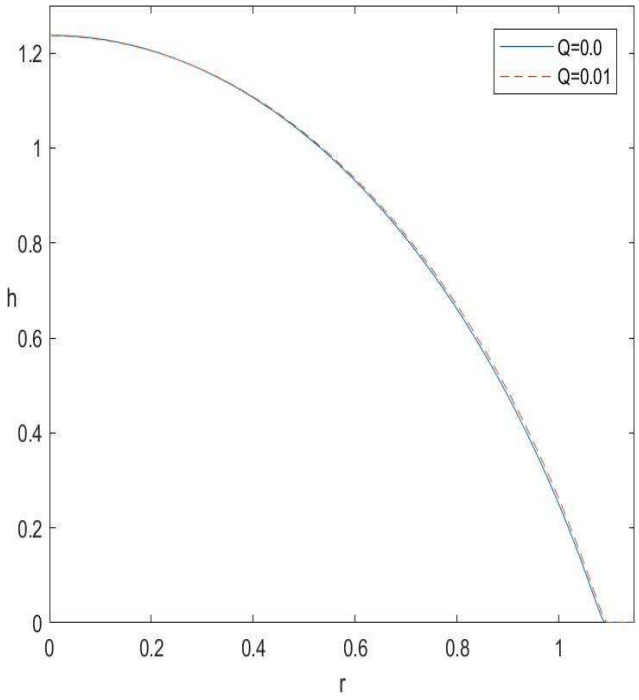

Figure 5.2: Interface comparison with varied value of the electric Weber number.

Interestingly, despite the change in evaporation rate and evaporative flux profile the interface itself remains largely unchanged with the addition of the electrostatic effects as seen in figure 5.2. Often the change in evaporative flux is an indication in change of contact angle or droplet shape as the droplet thickness adjusts the evaporation occurring at the contact angle. The fact that there is no change in interface shape leads to the conclusion that the change in evaporative flux is similar to that observed by the inclusion of localized

cooling of the substrate.

5.4. Conclusions

Electrostatic effects are added to the shear and normal stress conditions of an evaporating droplet. A mathematical model is derived and compared to that of a simpler model derived in Chapter 4. The electrostatic effects appear in the pressure gradient, shear stress condition, and in conjunction with the disjoining pressure. The second disjoining pressure term and localized cooling presented in the earlier droplet model are omitted. The electric Weber number is used to modify the strength of the effect of electrostatic forces on the droplet. It is found through preliminary results that unlike the modified disjoining pressure introduced in the earlier model the inclusion of the elctrostatic effects has little effect on droplet shape. However, similar to the localized cooling added into the relation of the interfacial temperature to heater power and evaporative flux, the electrostatic effects seem to increase evaporation time by lowering the value of the evaporative flux at the contact line.

Chapter 6

DISSERTATION CONTRIBUTION

The main contributions of this thesis are as follows:

- In Chapter 2 we introduce a variable heat transfer coefficient for the heat transfer problem of the CVB. This has never been done in the context of the CVB and gives valuable insight into the value of the internal heat transfer in different parts of the device. Following the analysis of the commonly used 1D model for heat transfer, a 2D and 3D adaptation of the models is presented building on the same key physical assumptions as used for the 1D model. A localized cooling effect is added to the boundary conditions in the 2D model allowing for adjustment of the heat transfer from the cuvette walls to aid in matching experimental data.

- In Chapter 3 insight is given into the flow of the heated region of the CVB through an analysis of evaporation and the steady-state configuration. Estimates of the flow velocity, not measured in experiments, are obtaned based on the mass conservation condition and the solution of the heat transfer problem. An analysis of Marangoni flow due to surface temperature gradient is discussed.

- In Chapter 4 a lubrication type model for a moving contact line is adapted to include an exponential term to the disjoining pressure approximating the effects of electrostatics. Comparison with experimental data is checked to verify the model, and the extra term gives more control over contact angle. Evaporative cooling of the substrate is incorporated into the model and is shown to decrease the evaporative flux near the contact line.

- In Chapter 5 we introduce a model for electrostatic effects on droplet evaporation building on the work of Ajaev [1] and Ketelaar and Ajaev [22]. Inclusion of electrostatic

effects in the context of droplet evaporation leads to decreased evaporative flux near the contact line.

The majority of the work contained in this thesis is presented in the following publications or preprints:

- James A. **Barrett** and Vladimir S. Ajaev. Modeling of Moving Liquid-Vapor Interfaces in the Constrained Vapor Bubble System. *Microgravity-Science and Technology*, 2019 DOI: 10.1007/s12217-019-09741-7

- James A. **Barrett** and Vladimir S. Ajaev. Heat Transfer and Corner Flow in the Constrained Vapor Bubble System *Interfacial Phenomena and Heat Transfer*, 2020 DOI: 10.1615/InterfacPhenomHeatTransfer.2020035445

- James A. **Barrett** and Vladimir S. Ajaev. Effect of electrostatic disjoining pressure on droplet evaporation. In preparation.

REFERENCES

[1] Ajaev, V. S. Spreading of thin volatile liquid droplets on uniformly heated surfaces. *Journal of Fluid Mechanics 528* (2005), 279–296.

[2] Ajaev, V. S. *Interfacial Fluid Mechanics: A Mathematical Modeling Approach*. Springer, New York, 2012.

[3] Ajaev, V. S., Gambaryan-Roisman, T., and Stephan, P. Static and dynamic contact angles of evaporating liquids on heated surfaces. *Journal of colloid and interface science 342*, 2 (2010), 550–558.

[4] Ajaev, V. S., and Homsy, G. M. Steady vapor bubbles in rectangular microchannels. *Journal of colloid and interface science 240*, 1 (2001), 259–271.

[5] Ancey, C. Plasticity and geophysical flows: a review. *Journal of Non-Newtonian Fluid Mechanics 142*, 1-3 (2007), 4–35.

[6] Anderson, D., and Davis, S. H. The spreading of volatile liquid droplets on heated surfaces. *Physics of Fluids 7*, 2 (1995), 248–265.

[7] Babin, B. R., Peterson, G. P., and Wu, D. Steady-state modeling and testing of a micro heat pipe. *Journal of heat transfer 112*, 3 (1990), 595–601.

[8] Barrett, J. A., and Ajaev, V. S. Modeling of moving liquid-vapor interfaces in the constrained vapor bubble system. *Microgravity Science and Technology 31*, 5 (2019), 685–692.

[9] Burelbach, J. P., Bankoff, S. G., and Davis, S. H. Nonlinear stability of evaporating/condensing liquid films. *Journal of Fluid Mechanics 195* (1988), 463–494.

[10] Chatterjee, A., Plawsky, J. L., Wayner Jr, P. C., Chao, D. F., Sicker, R. J., Lorik, T., Chestney, L., Eustace, J., and Zoldak, J. Constrained vapor bubble experiment for international space station: Earth's gravity results. *Journal of thermophysics and heat transfer 24*, 2 (2010), 400–410.

[11] Chatterjee, A., Plawsky, J. L., Wayner Jr, P. C., Chao, D. F., Sicker, R. J., Lorik, T., Chestney, L., Margie, R., Eustace, J., and Zoldak, J. Constrained vapor bubble heat pipe experiment aboard the international space station. *Journal of thermophysics and heat transfer 27*, 2 (2013), 309–319.

[12] Conroy, D., Craster, R., Matar, O., and Papageorgiou, D. Dynamics and stability of an annular electrolyte film. *Journal of Fluid Mechanics 656* (2010), 481–506.

[13] Cotter, T. P. Principles and prospects for micro heat pipes. Tech. rep., Los Alamos National Lab., NM (USA), 1984.

[14] Craster, R. V., and Matar, O. K. Dynamics and stability of thin liquid films. *Rev. Mod. Phys. 81* (2009), 1131.

[15] Davis, S. H., and Anderson, D. M. Spreading and evaporation of liquid drops on solids. In *Proceedings of the 1993 ASME Winter Annual Meeting* (1993), Publ by ASME, pp. 1–7.

[16] Derjaguin, B. Friction and adhesion. iv. the theory of adhesion of small particles. *Kolloid Zeits 69* (1934), 155–164.

[17] Derjaguin, B. V., and Churaev, N. *Surface forces*.

[18] Eijkel, J. C., and Van Den Berg, A. Nanofluidics: what is it and what can we expect from it? *Microfluidics and Nanofluidics 1*, 3 (2005), 249–267.

[19] Gokhale, S. J., Plawsky, J. L., and Wayner Jr, P. C. Experimental investigation of contact angle, curvature, and contact line motion in dropwise condensation and evaporation. *Journal of colloid and interface science 259*, 2 (2003), 354–366.

[20] Hindmarsh, A. C., Brown, P. N., Grant, K. E., Lee, S. L., Serban, R., Shumaker, D. E., and Woodward, C. S. SUNDIALS: Suite of nonlinear and differential/algebraic equation solvers. *ACM Transactions on Mathematical Software (TOMS) 31*, 3 (2005), 363–396.

[21] Huppert, H. E. Gravity currents: a personal perspective. *Journal of Fluid Mechanics 554* (2006), 299.

[22] Ketelaar, C., and Ajaev, V. S. Evaporation, viscous flow, and electrostatic interaction of charged interfaces in the apparent contact line region. *Physics of Fluids 27*, 11 (2015), 112110.

[23] Kirby, B. *Micro- and Nanoscale Fluid Mechanics: Transport in Microfluidic Devices*. Cambridge University Press, 2013.

[24] Kundan, A., Nguyen, T. T., Plawsky, J. L., Wayner Jr, P. C., Chao, D. F., and Sicker, R. J. Arresting the phenomenon of heater flooding in a wickless heat pipe in microgravity. *International Journal of Multiphase Flow 82* (2016), 65–73.

[25] Kundan, A., Plawsky, J. L., Wayner, P. C., Chao, D. F., Sicker, R. J., Motil, B. J., Lorik, T., Chestney, L., Eustace, J., and Zoldak, J. Thermocapillary phenomena and performance limitations of a wickless heat pipe in microgravity. *Phys. Rev. Lett. 114* (Apr 2015), 146105.

[26] Landau, L., Bell, J., Kearsley, M., Pitaevskii, L., Lifshitz, E., and Sykes, J. *Electrodynamics of Continuous Media*. COURSE OF THEORETICAL PHYSICS. Elsevier Science, 2013.

[27] Lide, D. *CRC Handbook of Chemistry and Physics, 85th Edition*. No. v. 85 in CRC Handbook of Chemistry and Physics, 85th Ed. Taylor & Francis, 2004.

[28] Luciani, S., Brutin, D., Le Niliot, C., Rahli, O., and Tadrist, L. Flow boiling in minichannels under normal, hyper-, and microgravity: local heat transfer analysis using inverse methods. *Journal of heat transfer 130*, 10 (2008).

[29] Margerit, J., Colinet, P., Lebon, G., Iorio, C. S., and Legros, J. C. Interfacial non-equilibrium and bénard-marangoni instability of a liquid-vapor system. *Phys. Rev. E 68* (Oct 2003), 041601.

[30] Markos, M., Ajaev, V. S., and Homsy, G. M. Steady flow and evaporation of a volatile liquid in a wedge. *Physics of Fluids 18*, 9 (2006), 092102.

[31] MathWorks, I. *Partial Differential Equation Toolbox 1: User's Guide : MATLAB.* MathWorks, Incorporated, 2006.

[32] Mazzoco, R. R., and Wayner Jr, P. C. Aqueous wetting films on fused quartz. *Journal of colloid and interface science 214*, 2 (1999), 156–169.

[33] Mehrizi, A. A., and Wang, H. Evaporating thin film profile near the contact line of a partially wetting water droplet under environmental heating. *International Journal of Heat and Mass Transfer,hindmarsh2005sundials*.

[34] Miladinova, S., Slavtchev, S., Lebon, G., and Legros, J.-C. Long-wave instabilities of non-uniformly heated falling films. *Journal of Fluid Mechanics 453* (2002), 153175.

[35] Moosman, S., and Homsy, G. Evaporating menisci of wetting fluids. *Journal of Colloid and Interface Science 73*, 1 (1980), 212–223.

[36] Oron, A., Bankoff, S. G., and Davis, S. H. Thermal singularities in film rupture. *Physics of Fluids 8*, 12 (1996), 3433–3435.

[37] Oron, A., Davis, S. H., and Bankoff, S. G. Long-scale evolution of thin liquid films. *Rev. Mod. Phys. 69* (1997), 931–980.

[38] Pohanish, R. *Sittig's Handbook of Toxic and Hazardous Chemicals and Carcinogens, 5th Edition*. EngineeringPro collection. Elsevier Science, 2008.

[39] Potash Jr, M., and Wayner Jr, P. Evaporation from a two-dimensional extended meniscus. *International Journal of Heat and Mass Transfer 15*, 10 (1972), 1851–1863.

[40] Reynolds, O. Iv. on the theory of lubrication and its application to mr. beauchamp towers experiments, including an experimental determination of the viscosity of olive oil. *Philosophical transactions of the Royal Society of London*, 177 (1886), 157–234.

[41] Saville, D. Electrohydrodynamics: the taylor-melcher leaky dielectric model. *Annual review of fluid mechanics 29*, 1 (1997), 27–64.

[42] Savino, R., and Paterna, D. Marangoni effect and heat pipe dry-out. *Physics of Fluids 18*, 11 (2006), 118103.

[43] Savino, R., Paterna, D., and Favaloro, N. Buoyancy and marangoni effects in an evaporating drop. *Journal of thermophysics and heat transfer 16*, 4 (2002), 562–574.

[44] Sodtke, C., Ajaev, V. S., and Stephan, P. Dynamics of volatile liquid droplets on heated surfaces: theory versus experiment. *Journal of Fluid Mechanics 610* (2008), 343.

[45] Swanson, L. W., and Peterson, G. P. The interfacial thermodynamics of micro heat pipes. *Journal of Heat Transfer 117*, 1 (1995), 195–201.

[46] Wu, D., and Peterson, G. P. Investigation of the transient characteristics of a micro heat pipe. *Journal of thermophysics and heat transfer 5*, 2 (1991), 129–134.

[47] Xu, X., and Carey, V. P. Film evaporation from a micro-grooved surface-an approximate heat transfer model and its comparison with experimental data. *Journal of Thermophysics and Heat Transfer 4*, 4 (1990), 512–520.

[48] Yang, L., and Homsy, G. M. Steady three-dimensional thermocapillary flows and dryout inside a v-shaped wedge. *Physics of Fluids 18*, 4 (2006), 042107.

[49] Yi, T., and Wong, H. Theory of slope-dependent disjoining pressure with application to lennard–jones liquid films. *Journal of colloid and interface science 313*, 2 (2007), 579–591.

[50] Zhang, H., Raghavan, V., and Gogos, G. Subcritical and supercritical droplet evaporation within a zero-gravity environment: Low weber number relative motion. *International Communications in Heat and Mass Transfer 35*, 4 (2008), 385–394.

[51] Zheng, L., Wang, Y.-X., Plawsky, J. L., and Wayner, P. C. Effect of curvature, contact angle, and interfacial subcooling on contact line spreading in a microdrop in dropwise condensation. *Langmuir 18*, 13 (2002), 5170–5177.